Chapter 3

Experiments with an insulating barrier and a flat base.

This chapter describes the results of a series of measurements performed with an annulus system fully blocked by a thermally insulating barrier, and with a flat base, giving the convection chamber constant depth.

Previous workers have shown that in an unblocked annulus the fluid heat transport decreases rapidly with increasing Ω (see *Figure 1.3*). The measurements reported in this chapter, using an annulus blocked by a radial barrier, confirm the findings of *Bowden and Eden (1968)*, which showed that the barrier modified the flow, so that the heat advection became largely independent of Ω – a result most unlike the unblocked flows. This thesis attempts to identify the processes responsible for maintaining the fluid heat transport. It has been possible to explain the mechanism by which one of these processes seems to work in this chapter, and chapter 5 explores two possible explanations for another of the processes.

Section 3.1 deals with the experimental measurements (including the heat transport results), which are summarized in section 3.1.3. The results are discussed in section 3.2. The flow is simplified to its basic components in §3.2.1, where the three basic processes by which the fluid advects heat are proposed.

The equations of heat advection for each of these components are derived (with appropriate simplifications) in §3.2.2. A mechanism for one component of the flow is put foward in §3.2.3 and tested in §3.2.4. The heat advection by other aspects of the flow is considered in §§3.2.5 and 3.2.6.

Conclusions about the nature of the flow are given in section 3.3, while 3.4 suggests how further investigations may be able to answer certain questions that arise from these experiments.

3.1 Experimental results.

3.1.1 Velocity measurements.

A regime diagram showing the values of τ and Θ for all the velocity measurements taken with the fully blocking thermally insulating barrier and flat base is shown in *Figure 3.1*. The measurements were taken at two values of ΔT, the upper line being those results where $\Delta T \approx 10\ K$ and the lower, $\Delta T \approx 4\ K$. Since $\Theta \propto \Omega^{-2}$ and $\tau \propto \Omega^2$, *Figure 3.1* shows low values of Ω at the top left corner and high values at the bottom right. It can be seen that eddies occur for $\Theta \lesssim 0.4$ and for $\tau \gtrsim 10^7$.

Figures 3.2 - 3.4 show measurements of horizontal velocities as a regular grid of vectors in an (r, ϕ)-plane. *Figure 3.2* was taken at $\Omega = 0.40\ rad.sec^{-1}$ and $\Delta T = 10.00\ K$. At the top of the annulus (a) strong radial flow can be seen away from the hot outer cylinder, towards the cold inner cylinder, while at the bottom of the annulus (e) the reverse can be seen. Prograde flow can be seen near the outer cylinder in (d) and (e), while retrograde flow appears near the inner cylinder in (b), (c), (d) and possibly (e). While measurements of vertical velocities were not available, continuity considerations suggest that fluid must be rising by the hot outer cylinder whilst moving in a prograde sense (at least in the lower regions), before flowing radially inwards at the top of the annulus. Fluid

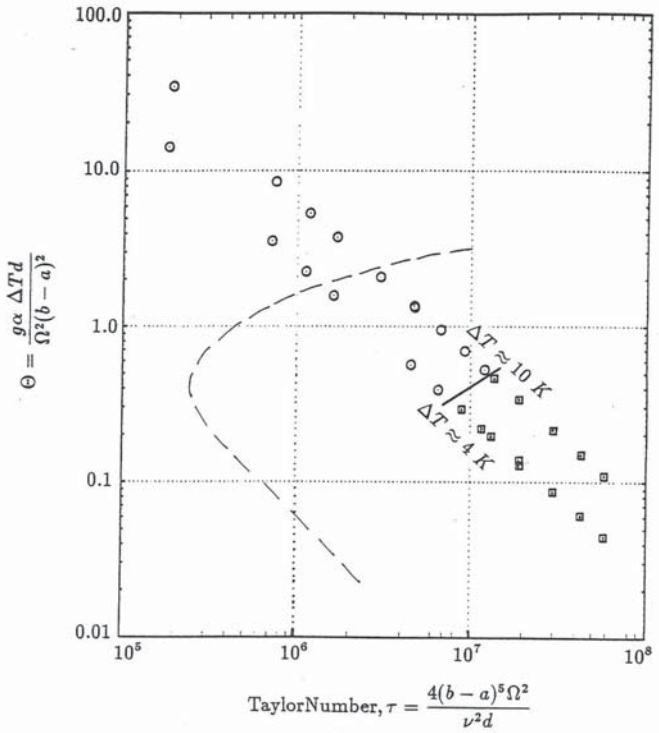

FIGURE 3.1: Regime diagram showing the values of τ and Θ for velocity runs 210-242, the measurements made with an insulating barrier and constant depth, $d = 140\ mm$. Measurements where no eddies were seen in the system are shown by circles, and measurements where eddies were seen are shown by squares. The dashed line indicates the approximate location of the transition for the onset of baroclinic waves in an unblocked annulus, such as that used by *Fowlis and Hide (1965)*. The location of the dashed line was obtained from D.W.Johnson (private communication), while the solid line indicates the transition for the onset of eddies in the present experiments.

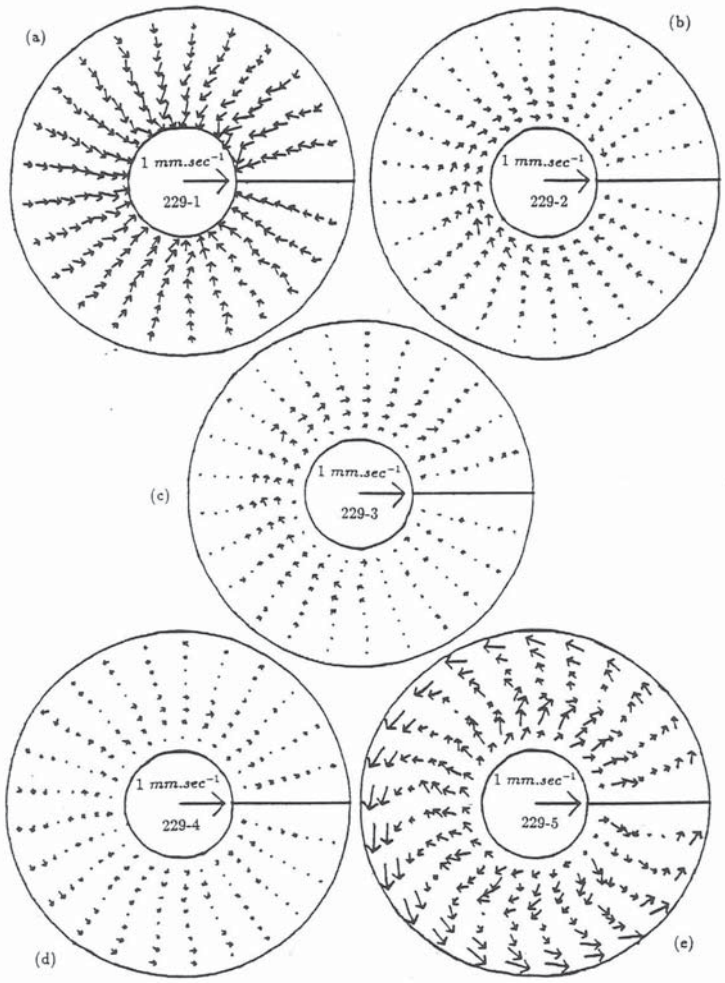

FIGURE 3.2: Horizontal velocity field data from VVAS reprojected onto a regular grid, for the annulus with a full thermally insulating barrier. The location of the barrier is indicated by the solid line in the 3 o'clock position. The flow is shown at various heights above the base of the annulus, these are; (a) 124mm, (b) 97mm, (c) 70mm, (d) 43mm, and (e) 16mm. Data from Run 229, $\Omega = 0.40\ rad.sec^{-1}$, $\Delta T = 10.00\ K$. In each case the central arrow depicts a velocity of 1 $mm.sec^{-1}$. The depth of the annulus was $d = 140\ mm$.

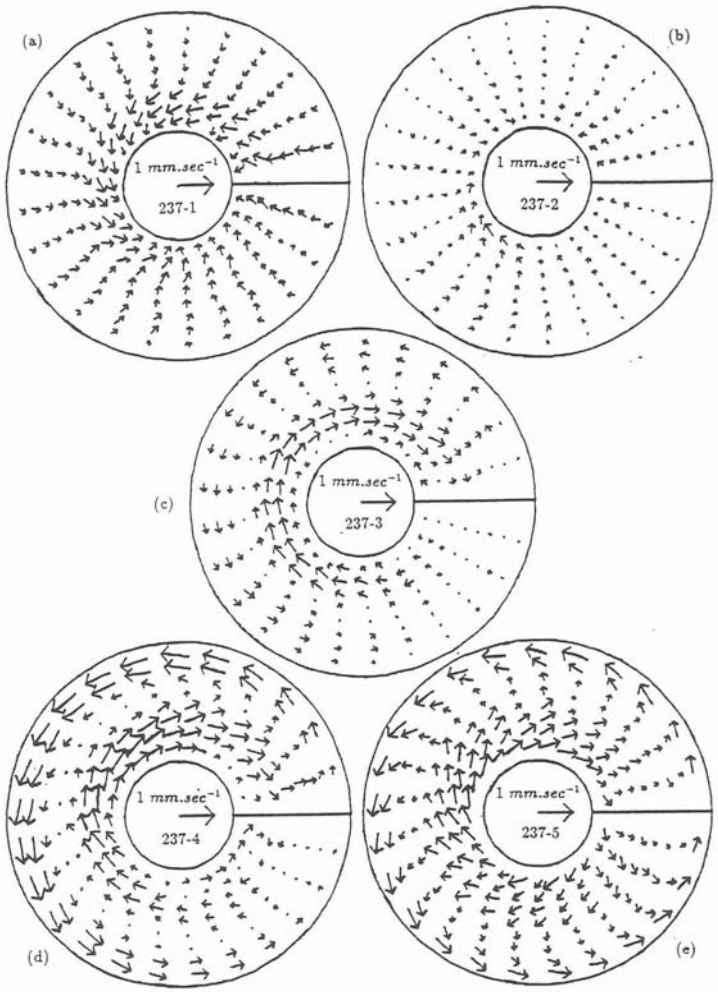

FIGURE 3.3: Horizontal velocity field data from VVAS reprojected onto a regular grid, for the annulus with a full thermally insulating barrier. The location of the barrier is indicated by the solid line in the 3 o'clock position. The flow is shown at various heights above the base of the annulus, these are; (a) 124mm, (b) 97mm, (c) 70mm, (d) 43mm, and (e) 16mm. Data from Run 237, Ω = 1.20 $rad.sec^{-1}$, $\Delta T = 10.09\ K$. In each case the central arrow depicts a velocity of 1 $mm.sec^{-1}$. The depth of the annulus was $d = 140\ mm$.

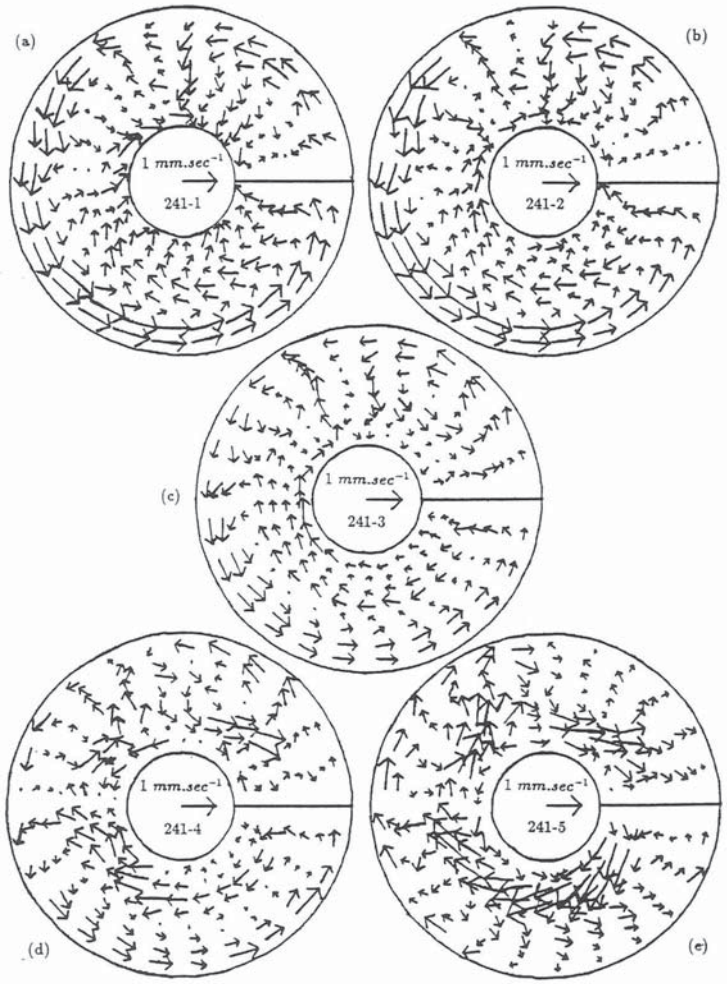

FIGURE 3.4: Horizontal velocity field data from VVAS reprojected onto a regular grid, for the annulus with a full thermally insulating barrier. The location of the barrier is indicated by the solid line in the 3 o'clock position. The flow is shown at various heights above the base of the annulus, these are; (a) 124mm, (b) 97mm, (c) 70mm, (d) 43mm, and (e) 16mm. Data from Run 241, Ω = 3.00 $rad.sec^{-1}$, $\Delta T = 9.98\ K$. In each case the central arrow depicts a velocity of 1 $mm.sec^{-1}$. The depth of the annulus was $d = 140\ mm$.

by the cold inner cylinder appears to be sinking and moving in a retrograde sense, before flowing radially outwards at the bottom of the annulus.

Figure 3.3 shows the fluid motions for $\Omega = 1.20\ rad.sec^{-1}$ and $\Delta T = 10.09\ K$. At this higher rotation rate the flow pattern is rather similar to that shown in *Figure 3.2*, with radial inflow at the top (a) and radial outflow at the bottom (e) of the annulus. The prograde flow near the outer cylinder and the retrograde flow by the inner cylinder appear to be stronger at this higher value of Ω.

Figure 3.4 shows results for $\Omega = 3.00\ rad.sec^{-1}$ and $\Delta T = 9.98\ K$. The flow has one or more eddies in it, but still appears to have the basic features of radial inflow near the top (a) and radial outflow near the bottom (e). Prograde flow can be seen by the outer cylinder at almost all heights (though not in (e)), while there is retrograde flow by the inner cylinder.

The azimuthal mean of the radial component of the fluid motions shown in *Figures 3.2 - 3.4* is more clearly shown in *Figure 3.5*, which shows contours of the radial component of velocity, u in an (r, z)-plane. (a) - (c) are the results for the values of Ω used in *Figures 3.2 - 3.4* respectively. *Figure 3.5* clearly shows the radial inflow at the top of the annulus and the radial outflow at the bottom. Also as the contours are approximately evenly spaced with z at mid-radius (particularly in (b) and (c)) this suggests that $\partial u/\partial z \approx constant$. It is worth noting that the magnitudes of u remain fairly constant with Ω, a result which is likely to be significant in terms of the heat transported by advection through the annulus.

The mean over azimuth of the azimuthal component of the fluid motions is shown in *Figure 3.6*, where contours of the azimuthal component of velocity, v in an (r, z)-plane can be seen. (a) - (c) are the results for the values of Ω used in *Figures 3.2 - 3.4* respectively. The flow patters are quite complex, showing both radial and vertical shear. However it is clear that the magnitude of v increases

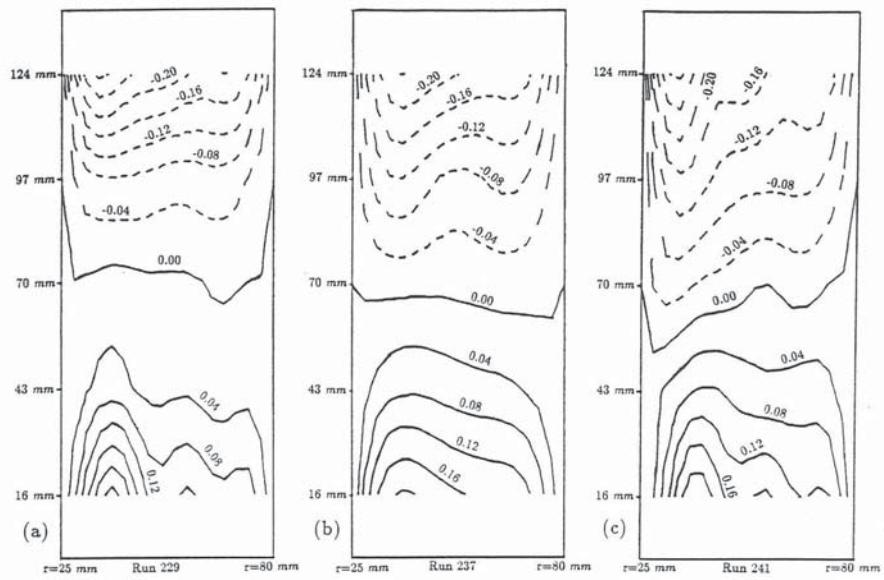

FIGURE 3.5: The figures show contours of the azimuthal mean of the radial component of velocity in an (r, z) plane, for the system with an insulating barrier and constant depth, $d = 140\ mm$. Solid contours represent radially outwards flow and dashed contours, inwards flow. (a) Run 229, $\Delta T = 10.00\ K$, $\Omega = 0.400\ rad.sec^{-1}$, (b) Run 237, $\Delta T = 10.09\ K$, $\Omega = 1.196\ rad.sec^{-1}$, and (c) Run 241, $\Delta T = 9.98\ K$, $\Omega = 3.003\ rad.sec^{-1}$. In all cases a clear shear of radial velocity with z can be seen, which is suggestive of radial overturning. In (b) and (c) the even spacing of the contours with z at mid-radius indicates that $\partial u/\partial z \approx constant$.

significantly as Ω increases.

Figure 3.7 shows contours of the radial component of velocity, u in a (ϕ, z)-plane at mid-radius, where (a) - (c) again correspond to the results seen in *Figures 3.2 - 3.4*. In (a) and (b) the shear of u with z can again be seen, as well as (particularly in (b)) a shear of u with ϕ. In (c) there are areas where the shear of u with z and ϕ can be clearly seen, but also there is a localized region where

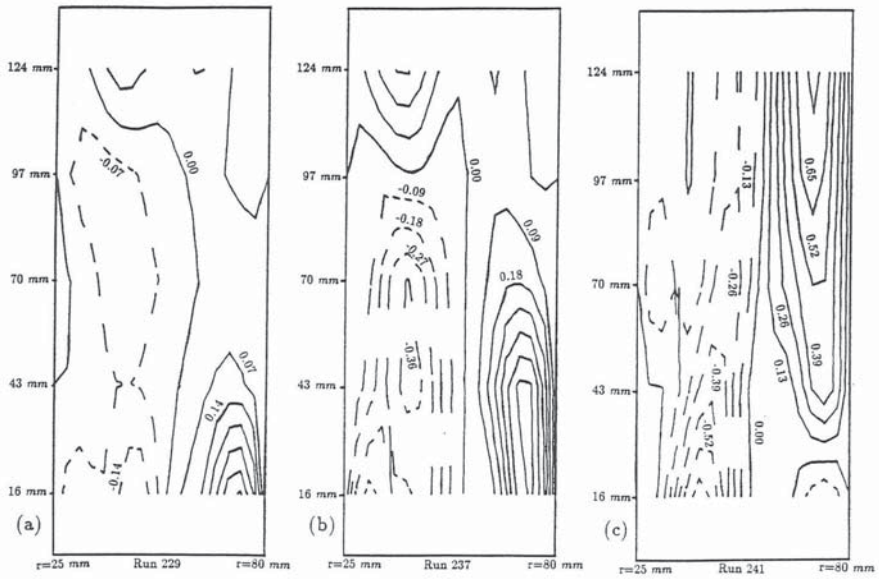

FIGURE 3.6: The figures show contours of the mean over ϕ of v in an (r, z) plane for the annulus with a full insulating barrier and depth, $d = 140$ *mm*. Solid contours represent prograde flow and dashed contours retrograde flow. (a) Run 229, $\Delta T = 10.00$ *K*, $\Omega = 0.400$ *rad.sec*$^{-1}$; (b) run 237, $\Delta T = 10.09$ *K*, $\Omega = 1.196$ *rad.sec*$^{-1}$; and (c) run 241, $\Delta T = 9.98$ *K*, $\Omega = 3.003$ *rad.sec*$^{-1}$. The flow patterns appear to be quite complex with both radial and vertical shear. At mid-height ($z = 0$) the shear of v appears to increase with Ω.

u has strong dependence on ϕ, which would appear to correspond to a localized eddy, with little vertical structure. This is characteristic of the sort of eddies seen at higher rotation rates in the system.

The velocity results are summarized in *Table 3.1*, which in addition to various control parameters and non-dimensional numbers indicates whether eddies were present or not during a measurement under the heading of 'flow type'.

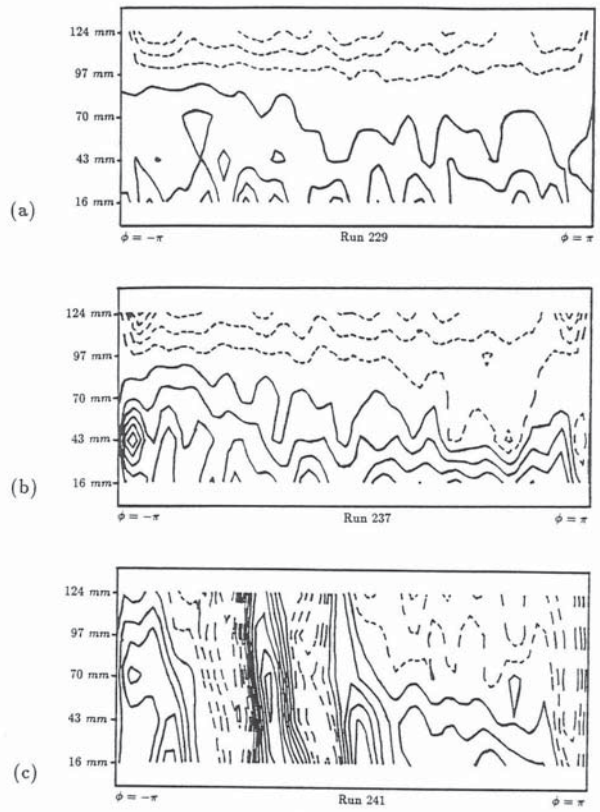

FIGURE 3.7: The figures show contours of u in a (ϕ, z) plane for the annulus with a full insulating barrier. Solid contours represent radially outwards flow and dashed contours, inwards flow. (a) Run 229, $\Delta T = 10.00$ *K*, $\Omega = 0.40$ *rad.sec*$^{-1}$, contour interval 0.08 *mm.sec*$^{-1}$. (b) Run 237, $\Delta T = 10.09$ *K*, $\Omega = 1.20$ *rad.sec*$^{-1}$, contour interval 0.07 *mm.sec*$^{-1}$, and (c) Run 241, $\Delta T = 9.98$ *K*, $\Omega = 3.00$ *rad.sec*$^{-1}$, contour interval 0.12 *mm.sec*$^{-1}$.

Run No	ΔT K	Ω $rad.sec^{-1}$	Prandtl No	Θ	Taylor No	Rayleigh No	Ekman No	Flow type
210	4.03	0.489	13.6	2.26	1.12×10^6	8.60×10^6	5.93×10^{-4}	no eddies
211	4.04	0.195	13.6	1.43×10^1	1.78×10^5	8.62×10^6	1.49×10^{-3}	no eddies
212	4.07	0.391	13.6	3.58	7.15×10^5	8.69×10^6	7.41×10^{-4}	no eddies
213	4.07	0.589	13.6	1.59	1.61×10^6	8.69×10^6	4.94×10^{-4}	no eddies
215	4.05	0.980	13.6	5.67×10^{-1}	4.49×10^6	8.64×10^6	2.96×10^{-4}	no eddies
216	4.06	1.176	13.6	3.94×10^{-1}	6.47×10^6	8.66×10^6	2.46×10^{-4}	no eddies
217	4.05	1.372	13.6	2.89×10^{-1}	8.80×10^6	8.64×10^6	2.11×10^{-4}	eddies
218	4.05	1.569	13.6	2.21×10^{-1}	1.15×10^7	8.64×10^6	1.85×10^{-4}	eddies
219	4.03	1.665	13.6	1.95×10^{-1}	1.30×10^7	8.60×10^6	1.74×10^{-4}	eddies
220	4.07	1.666	13.6	1.97×10^{-1}	1.30×10^7	8.69×10^6	1.74×10^{-4}	eddies
221	3.79	2.000	13.6	1.27×10^{-1}	1.87×10^7	8.69×10^6	1.45×10^{-4}	eddies
222	4.04	2.500	13.6	8.69×10^{-2}	2.92×10^7	8.62×10^6	1.16×10^{-4}	eddies
223	4.04	2.000	13.6	1.36×10^{-1}	1.87×10^7	8.62×10^6	1.45×10^{-4}	eddies
224	4.05	1.999	13.6	1.36×10^{-1}	1.87×10^7	8.64×10^6	1.45×10^{-4}	eddies
225	4.09	3.503	13.6	4.48×10^{-2}	5.74×10^7	8.73×10^6	8.28×10^{-5}	eddies
226	4.08	3.002	13.6	6.08×10^{-2}	4.21×10^7	8.71×10^6	9.66×10^{-5}	eddies
227	10.01	0.500	13.6	5.38	1.17×10^6	2.14×10^7	5.80×10^{-4}	no eddies
228	10.00	0.200	13.6	3.36×10^1	1.87×10^5	2.13×10^7	1.45×10^{-3}	no eddies
229	10.00	0.400	13.6	8.42	7.47×10^5	2.13×10^7	7.26×10^{-4}	no eddies
230	9.99	0.599	13.6	3.74	1.68×10^6	2.13×10^7	4.84×10^{-4}	no eddies
231	9.97	0.799	13.6	2.10	2.99×10^6	2.13×10^7	3.63×10^{-4}	no eddies
232	9.98	1.000	13.6	1.34	4.68×10^6	2.13×10^7	2.90×10^{-4}	no eddies
233	10.07	1.196	13.6	9.45×10^{-1}	6.69×10^6	2.15×10^7	2.42×10^{-4}	no eddies
234	10.08	1.402	13.6	6.88×10^{-1}	9.20×10^6	2.15×10^7	2.07×10^{-4}	no eddies
235	10.01	1.598	13.6	5.26×10^{-1}	1.20×10^7	2.14×10^7	1.81×10^{-4}	no eddies
236	10.10	1.000	13.6	1.36	4.68×10^6	2.16×10^7	2.90×10^{-4}	no eddies
237	10.09	1.196	13.6	9.47×10^{-1}	6.69×10^6	2.15×10^7	2.42×10^{-4}	no eddies
238	9.93	1.697	13.6	4.64×10^{-1}	1.35×10^7	2.12×10^7	1.71×10^{-4}	eddies
239	9.98	2.000	13.6	3.35×10^{-1}	1.87×10^7	2.13×10^7	1.45×10^{-4}	eddies
240	10.00	2.500	13.6	2.15×10^{-1}	2.92×10^7	2.13×10^7	1.16×10^{-4}	eddies
241	9.98	3.003	13.6	1.49×10^{-1}	4.22×10^7	2.13×10^7	9.65×10^{-5}	eddies
242	9.96	3.504	13.6	1.09×10^{-1}	5.74×10^7	2.13×10^7	8.27×10^{-5}	eddies

TABLE 3.1: Velocity measurements with a full thermally insulating barrier and a flat base.

3.1.2 Heat and temperature measurements.

A regime diagram showing the values of Θ and τ for all the temperature and heat transport measurements is shown in *Figure 3.8*. Comparison with *Figure 3.1* shows that the transition for the onset of eddies was found to occur at similar values to those seen using velocity measurements.

Figure 3.9 shows the fluid temperature measured by the thermocouple ring at mid-radius ($r = \bar{r}$), and mid-height ($z = 0$) as a function of ϕ, $T(\bar{r}, z = 0; \phi, t)$. The barrier was placed at $\phi = \pm\pi$. Plots of temperature are given for three values of Ω for each of the two values of ΔT used. It can be seen that $\partial T(\bar{r}, z = 0; \phi)/\partial\phi \approx$ *constant* over most rotation rates, although 'kinks' appear at higher values of Ω in some cases. The temperature drop across the barrier, ΔT_B can be seen to increase with Ω.

The dependence of ΔT_B on Ω can be seen more clearly in *Figure 3.10*, which shows plots of ΔT_B against Ω for the two values of ΔT used in the experiments. It can be seen that ΔT_B increases approximately linearly with Ω before levelling off at a value of 20 - 25 % of ΔT.

The total heat transport of the fluid as expressed by the Nusselt number, Nu(Ω) is shown in *Figure 3.11*. The plots show Nu(Ω)/Nu($\Omega = 0$) against Ω, for the two values of ΔT used. Both sets of results show that the Nusselt number (and therefore the advective heat transport by the fluid) remains fairly constant with Ω, at approximately the same value as when $\Omega = 0$ but increases (at $\Delta T \approx 10\ K$) for Ω above about 1.2 $rad.sec^{-1}$ to reach a maximum about 7% higher than at $\Omega = 0$. *Table 3.1* shows that eddies occured for Ω larger than 1.2 to 1.7 $rad.sec^{-1}$. When $\Delta T = 4\ K$, Nu(Ω)$\approx$ Nu($\Omega = 0$) to within the accuracy of the error bars.

Table 3.2 summarizes the temperature and heat transport results, showing the total heat conduction by the fluid in addition to the total heat transport by

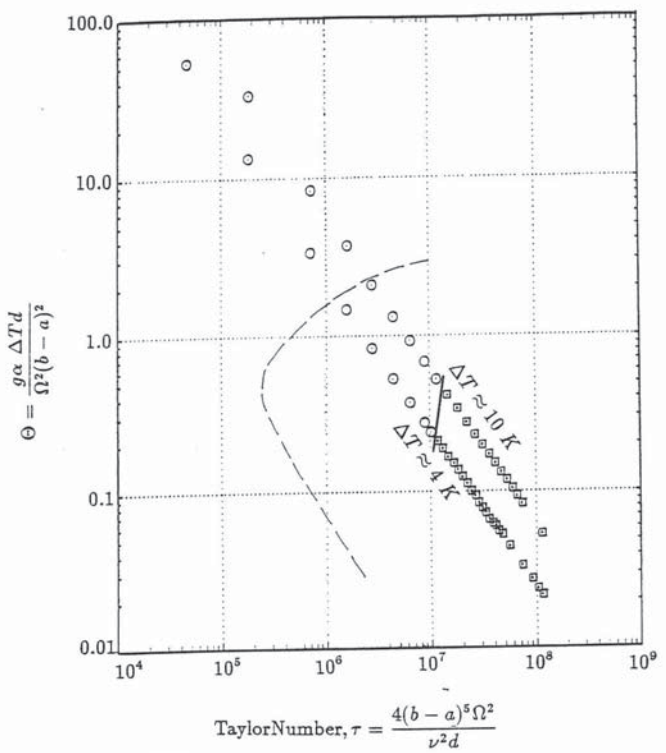

FIGURE 3.8: Regime diagram showing the values of τ and Θ for Runs 4U-9L, the measurements made with an insulating barrier and constant depth, $d = 140\ mm$. The circles show values where temperature measurements indicated that there were no eddies in the system, and the squares show values where eddies were present. The dashed line indicates the approximate location of the transition for the onset of baroclinic waves in an unblocked annulus, such as that used by *Fowlis and Hide (1965)*. The location of the dashed line was obtained from D.W.Johnson (private communication), while the solid line indicates the transition for the onset of eddies in the present experiments.

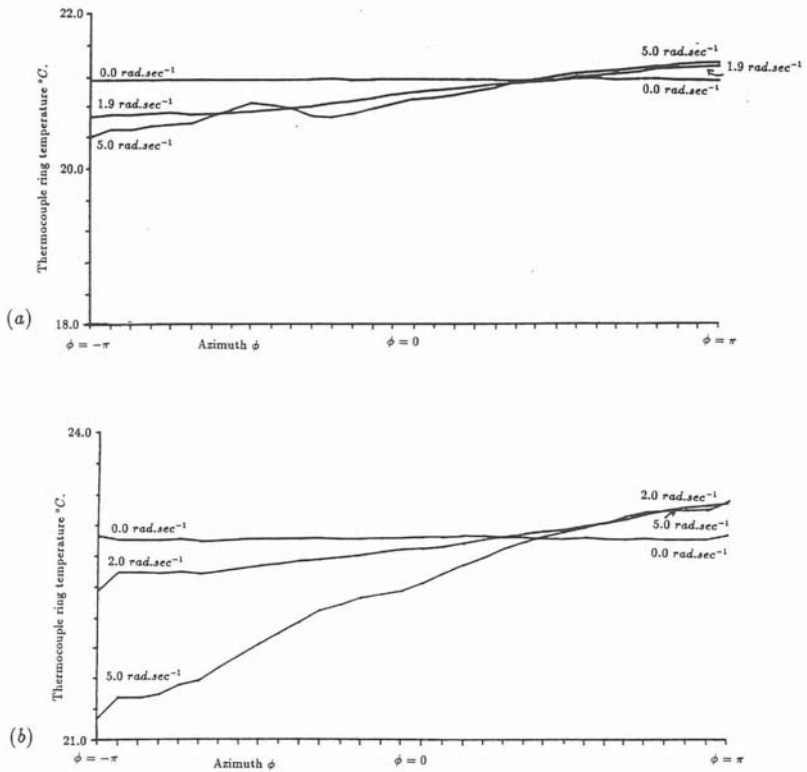

FIGURE 3.9: Experimental results showing temperature of ring thermocouple against azimuthal position for three rotation rates, $\Omega = 0.0, 1.9$(or 2.0) and $5.0\ rad.sec^{-1}$, for the system with constant depth, $d = 140\ mm$ and the full thermally insulating barrier. Each of the scale markings along the horizontal axis shows the location of one of the thermocouples in the ring. Measurements of temperature were taken for each thermocouple in the ring, with a straight line drawn between them as a guide to the eye. The standard errors were $0.014°C$ in both cases. The externally applied temperature differences were (a) $\Delta T \approx 4\ K$, (b) $\Delta T \approx 10\ K$. $\Delta T_B(\Omega)$ was defined as the difference between the maximum and minimum thermocouple ring temperatures for a given Ω. As the figures show ΔT_B was generally the temperature difference between one side of the barrier and the other.

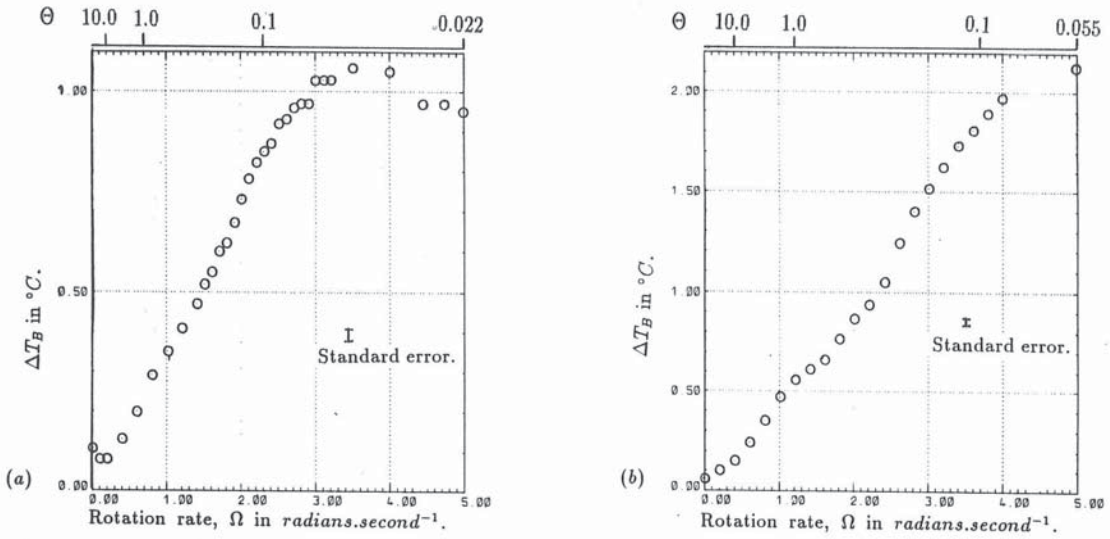

FIGURE 3.10: Experimental results showing dependence of ΔT_B on Ω, for the system with a full thermally insulating barrier and depth, $d = 140\ mm$. The externally applied temperature differences were (a) $\Delta T \approx 4\ K$ and (b) $\Delta T \approx 10\ K$.

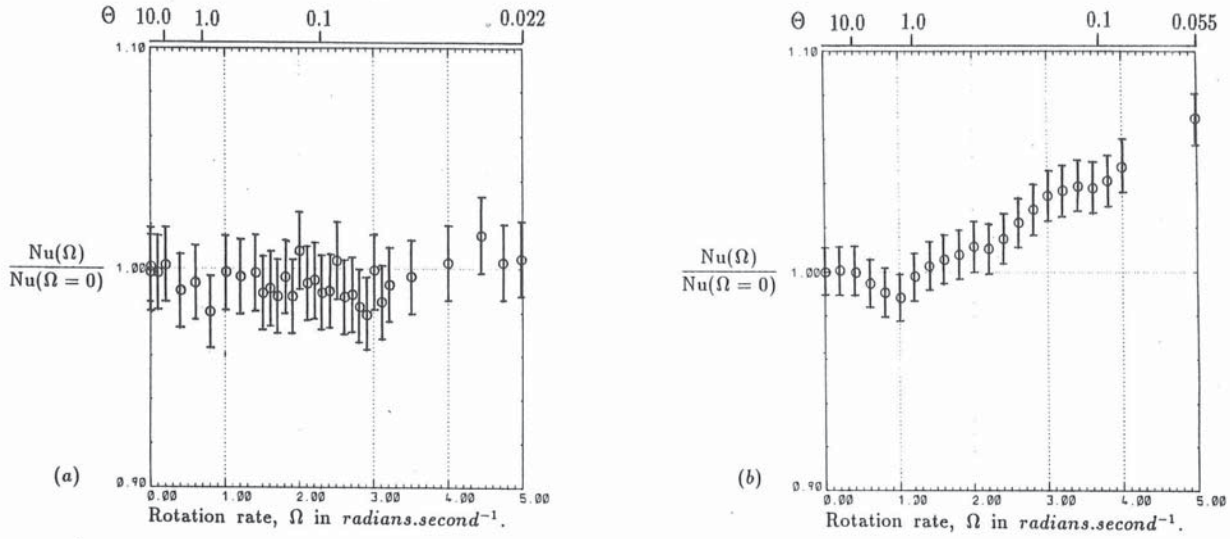

FIGURE 3.11: Experimental results showing the dependence of $\mathrm{Nu}(\Omega)/\mathrm{Nu}(\Omega = 0)$ on Ω, for the system with a full thermally insulating radial barrier and depth, $d = 140\ mm$. The externally applied temperature differences were (a) $\Delta T \approx 4\ K$ and (b) $\Delta T \approx 10\ K$.

TABLE 3.2: Temperature and heat transport measurements for the annulus with a fully blocking, thermally insulating barrier.

Run No	Number of results	ΔT K	Ω $rad.sec^{-1}$	ΔT_{BAR} K	Prandtl No	Θ	Taylor No	Rayleigh No	Ekman No	$H_{conductive}$ $watts$	H_{total} $watts$	Nusselt No
4U	131	4.02	0.000	0.11	13.82	∞	0	8.43×10^6	∞	1.59	17.67	11.14
4V	131	4.01	0.101	0.08	13.82	5.28×10^1	4.61×10^4	8.41×10^6	2.92×10^{-3}	1.58	17.56	11.10
4W	131	4.03	0.201	0.08	13.82	1.34×10^1	1.83×10^5	8.46×10^6	1.47×10^{-3}	1.59	17.72	11.14
4X	126	4.03	0.401	0.13	13.82	3.37	7.27×10^5	8.47×10^6	7.53×10^{-4}	1.59	17.54	11.01
4Y	131	3.95	0.601	0.20	13.82	1.47	1.63×10^6	8.30×10^6	4.91×10^{-4}	1.56	17.26	11.05
5A	119	3.99	0.801	0.29	13.82	8.35×10^{-1}	2.90×10^6	8.37×10^6	3.68×10^{-4}	1.57	17.16	10.90
5B	241	3.96	1.006	0.35	13.82	5.26×10^{-1}	4.57×10^6	8.31×10^6	2.93×10^{-4}	1.56	17.35	11.10
5C	241	4.00	1.205	0.41	13.82	3.70×10^{-1}	6.56×10^6	8.38×10^6	2.45×10^{-4}	1.58	17.48	11.08
5D	181	4.04	1.406	0.47	13.82	2.74×10^{-1}	8.94×10^6	8.48×10^6	2.10×10^{-4}	1.59	17.71	11.10
5E	241	4.03	1.606	0.55	13.82	2.10×10^{-1}	1.17×10^7	8.45×10^6	1.84×10^{-4}	1.59	17.51	11.02
5F	241	4.00	1.806	0.62	13.82	1.65×10^{-1}	1.47×10^7	8.40×10^6	1.63×10^{-4}	1.58	17.50	11.08
5G	441	4.10	2.005	0.73	13.82	1.37×10^{-1}	1.82×10^7	8.60×10^6	1.47×10^{-4}	1.62	18.13	11.21
5H	481	3.98	2.505	0.92	13.82	8.52×10^{-2}	2.84×10^7	8.35×10^6	1.18×10^{-4}	1.57	17.53	11.16
5J	481	3.99	3.003	1.03	13.82	5.95×10^{-2}	4.08×10^7	8.38×10^6	9.82×10^{-5}	1.58	17.52	11.11
7R	133	4.05	0.000	0.03	13.82	∞	0	8.50×10^6	∞	1.60	17.74	11.10
7S	551	4.04	3.500	1.06	13.82	4.43×10^{-2}	5.54×10^7	8.47×10^6	8.42×10^{-5}	1.59	17.67	11.08
7T	359	4.01	3.996	1.05	13.82	3.38×10^{-2}	7.22×10^7	8.42×10^6	7.38×10^{-5}	1.58	17.65	11.15
7U	521	4.02	4.443	0.97	13.82	2.74×10^{-2}	8.92×10^7	8.43×10^6	6.64×10^{-5}	1.59	17.91	11.29
7V	241	4.02	1.506	0.52	13.82	2.38×10^{-1}	1.03×10^7	8.44×10^6	1.96×10^{-4}	1.59	17.46	11.00
7W	241	4.04	1.706	0.60	13.82	1.87×10^{-1}	1.32×10^7	8.49×10^6	1.73×10^{-4}	1.60	17.53	10.98
7X	241	4.03	1.905	0.67	13.82	1.49×10^{-1}	1.68×10^7	8.45×10^6	1.55×10^{-4}	1.59	17.45	10.98
7Y	421	4.06	2.105	0.78	13.82	1.23×10^{-1}	2.00×10^7	8.52×10^6	1.40×10^{-4}	1.60	17.72	11.05
8A	241	4.04	2.205	0.82	13.82	1.12×10^{-1}	2.20×10^7	8.48×10^6	1.34×10^{-4}	1.59	17.64	11.06
8B	361	3.97	2.305	0.85	13.82	1.00×10^{-1}	2.40×10^7	8.33×10^6	1.28×10^{-4}	1.57	17.23	11.00
8C	441	3.97	2.405	0.87	13.82	9.23×10^{-2}	2.61×10^7	8.34×10^6	1.23×10^{-4}	1.57	17.27	11.01
8D	361	3.96	2.605	0.93	13.82	7.84×10^{-2}	3.07×10^7	8.31×10^6	1.13×10^{-4}	1.56	17.17	10.98
8E	401	3.95	2.705	0.96	13.82	7.26×10^{-2}	3.31×10^7	8.30×10^6	1.09×10^{-4}	1.56	17.16	10.99
8F	401	3.93	2.805	0.97	13.82	6.72×10^{-2}	3.56×10^7	8.25×10^6	1.05×10^{-4}	1.55	16.94	10.93
8G	401	3.92	2.905	0.97	13.82	6.24×10^{-2}	3.81×10^7	8.23×10^6	1.01×10^{-4}	1.55	16.86	10.89
8H	401	4.01	3.104	1.03	13.82	5.59×10^{-2}	4.35×10^7	8.42×10^6	9.50×10^{-5}	1.58	17.33	10.95
8J	361	4.02	3.203	1.03	13.82	5.26×10^{-2}	4.64×10^7	8.43×10^6	9.20×10^{-5}	1.59	17.50	11.04
8K	361	4.00	4.980	0.95	13.82	2.17×10^{-2}	1.12×10^8	8.39×10^6	5.92×10^{-5}	1.58	17.64	11.17
8L	361	3.99	4.738	0.97	13.82	2.39×10^{-2}	1.01×10^8	8.36×10^6	6.22×10^{-5}	1.57	17.55	11.15

TABLE 3.2 (Continued.)

Run No	Number of results	ΔT K	Ω $rad.sec^{-1}$	ΔT_{BAR} K	Prandtl No	Θ	Taylor No	Rayleigh No	Ekman No	$H_{conductive}$ $watts$	H_{total} $watts$	Nusselt No
8M	121	10.01	0.000	0.06	13.82	∞	0	2.10×10^7	∞	3.95	54.86	13.88
8N	121	10.02	0.202	0.10	13.82	3.30×10^1	1.84×10^5	2.10×10^7	1.46×10^{-3}	3.95	54.94	13.89
8P	121	9.98	0.402	0.15	13.82	8.30	7.30×10^5	2.09×10^7	7.33×10^{-4}	3.94	54.68	13.88
8R	241	9.98	0.602	0.24	13.82	3.70	1.64×10^6	2.09×10^7	4.90×10^{-4}	3.94	54.44	13.81
8S	241	9.96	0.802	0.35	13.82	2.08	2.90×10^6	2.09×10^7	3.68×10^{-4}	3.93	54.06	13.75
8T	241	9.98	1.006	0.47	13.82	1.33	4.57×10^6	2.09×10^7	2.93×10^{-4}	3.94	54.08	13.72
8U	241	10.00	1.206	0.56	13.82	9.23×10^{-1}	6.57×10^6	2.10×10^7	2.44×10^{-4}	3.95	54.65	13.85
8V	241	9.99	1.406	0.61	13.82	6.79×10^{-1}	8.94×10^6	2.10×10^7	2.10×10^{-4}	3.95	54.93	13.92
8W	241	9.98	1.605	0.66	13.82	5.20×10^{-1}	1.16×10^7	2.09×10^7	1.84×10^{-4}	3.94	55.01	13.96
8X	241	9.99	1.806	0.77	13.82	4.11×10^{-1}	1.47×10^7	2.10×10^7	1.63×10^{-4}	3.94	55.14	13.99
8Y	241	10.06	2.005	0.87	13.82	3.36×10^{-1}	1.82×10^7	2.11×10^7	1.47×10^{-4}	3.97	55.77	14.04
9A	301	9.98	2.205	0.94	13.82	2.76×10^{-1}	2.20×10^7	2.09×10^7	1.34×10^{-4}	3.94	55.27	14.03
9B	301	9.96	2.405	1.05	13.82	2.31×10^{-1}	2.61×10^7	2.09×10^7	1.23×10^{-4}	3.93	55.43	14.09
9C	301	9.95	2.604	1.24	13.82	1.97×10^{-1}	3.07×10^7	2.09×10^7	1.13×10^{-4}	3.93	55.76	14.19
9D	301	9.96	2.804	1.40	13.82	1.70×10^{-1}	3.55×10^7	2.09×10^7	1.05×10^{-4}	3.93	56.15	14.27
9E	401	10.03	3.003	1.52	13.82	1.49×10^{-1}	4.08×10^7	2.10×10^7	9.82×10^{-5}	3.96	56.85	14.36
9F	401	10.04	3.202	1.63	13.82	1.32×10^{-1}	4.63×10^7	2.11×10^7	9.21×10^{-5}	3.96	57.02	14.39
9G	401	10.05	3.402	1.73	13.82	1.17×10^{-1}	5.23×10^7	2.11×10^7	8.67×10^{-5}	3.97	57.22	14.42
9H	401	9.95	3.601	1.81	13.82	1.03×10^{-1}	5.86×10^7	2.09×10^7	8.19×10^{-5}	3.93	56.59	14.41
9J	401	9.94	3.799	1.89	13.82	9.25×10^{-2}	6.52×10^7	2.09×10^7	7.76×10^{-5}	3.92	56.70	14.45
9K	401	9.95	3.996	1.97	13.82	8.38×10^{-2}	7.22×10^7	2.09×10^7	7.38×10^{-5}	3.93	57.12	14.54
9L	551	9.93	4.985	2.13	13.82	5.37×10^{-2}	1.12×10^8	2.08×10^7	5.91×10^{-5}	3.92	58.15	14.84

the fluid and the Nusselt number for each measurement.

3.1.3 Summary of results.

The observed flow for an annulus with a fully blocking thermally insulating barrier appears to consist of three main components: (1) a radial overturning in which $\partial u/\partial z \approx constant$, (2) a circulation in the horizontal (which has some vertical structure however) which manifests itself as prograde flow by the outer cylinder and retrograde flow by the inner cylinder, and (3) eddies which appear at higher values of Ω and are seen at values of $\Theta \lesssim 0.4$ and values of $\tau \gtrsim 10^7$.

A temperature drop, ΔT_B is observed across the barrier for all values of $\Omega \neq 0$. ΔT_B appears to increase linearly with Ω until a maximum is reached at a value of about 20% to 25% of the applied ΔT. This maximum is reached at a value of $\Theta \sim 6 \times 10^{-2}$ or 8×10^{-2}.

The total heat transported by the fluid remained fairly constant against Ω at the $\Omega = 0$ value, though at $\Delta T \approx 10\ K$ a gradual increase with Ω was seen above 1.2 $rad.sec^{-1}$ which corresponded to the range of Ω over which eddies were seen.

3.2 Discussion of results.

3.2.1 Simplified interpretation of flow pattern.

Excluding the eddies, the interpretation of the experimental results can be considerably simplified by regarding the fluid motions as the superposition of two circulations. These circulations are illustrated schematically by *Figure 3.12.* The first is a radial overturning cell, characterized by $\partial u/\partial z \approx constant$. The axis of this circulation lies antiparallel to $\hat{\phi}$, the unit azimuthal vector, and by analogy with the components of the relative vorticity vector $\vec{\omega} = (\xi, \eta, \zeta)$ shall be denoted the η-circulation. The second circulation is assumed to be independent of z and lies in a horizontal plane, using the same thinking as above it shall be known as

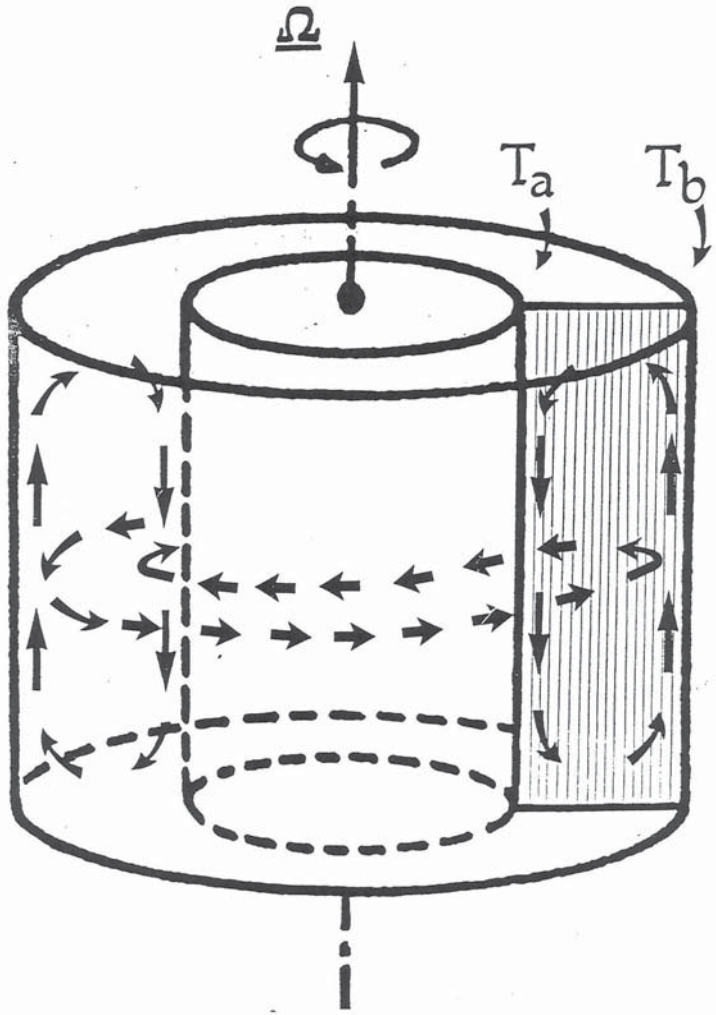

FIGURE 3.12: Diagram illustrating the simplified flow pattern representing fluid motions for the results described in section 3.1. The velocity measurements when there are no eddies are represented by the two circulations shown by the arrows. The radial overturning cell, which is independent of ϕ, is called the η-circulation, while the horizontal circulation, which is independent of z is called the ζ-circulation. These circulations represent a useful simplification to the observed flows when eddies are absent.

the ζ-circulation.

Both these circulations contribute to radial motions in the fluid, and so may contribute to the advective heat transport by the fluid. By use of this simplification, the problem of understanding how the fluid maintains the heat transport reduces to that of finding the mechanisms for the two circulations, and the heat transport contributions of each of the circulations and the eddies.

3.2.2 Heat transport considerations.

The experiments measured the total heat transported by the fluid, $H_{total} = H_{cond} + H_{adv}$. The advective heat transport could therefore be obtained by subtracting the conductive heat transport,

$$H_{cond} = \frac{2\pi k \Delta T d}{\ln(b/a)}$$

from H_{total}. The net heat transport through a surface $\mathcal{S}$ by advection is

$$H_{adv}(r,\phi,z,t) = \int_{\mathcal{S}} \vec{H}_{adv}(r,\phi,z,t).d\vec{\mathcal{S}}, \qquad (3.1)$$

hence if the temperature and velocity fields for the fluid motions are known, the advective heat transport may be calculated from them for comparison with the experimental results. In practice it was not possible to measure the entire temperature field, $T(r,\phi,z,t)$, and the velocity field data was limited by its accuracy. The approach followed for the temperature field was to use the limited data available, $T(\bar{r}, z=0;\phi,t)$ with appropriate approximations. The velocity field data was used to attempt to identify the mechanisms for the flow, so that the fluid velocities could be calculated using appropriate theory, from the more accurate temperature field data, and various experimental parameters. It proved possible to identify the mechanism for the η-circulation, however the mechanism for the ζ-circulation proved more elusive, so that velocity data had to be used to estimate its heat transport contribution.

The total advective heat transport is given by equation (3.1) where $\vec{H}_{adv}$ is given by equation (1.4) and the direction of $d\vec{\mathcal{S}}$ is normal to the surface $\mathcal{S}$. If the lid and base of the annulus were perfect insulators, the heat advected through the annulus (and measured at the inner cylinder) must have passed through a cylindrical surface of height d at mid-radius, $\bar{r} = \frac{1}{2}(a+b)$. In this case the normal to the surface is parallel to $\hat{r}$, the unit vector in the r-direction, so that $d\vec{\mathcal{S}} = \hat{r}\bar{r}d\phi dz$. As $\vec{u} = (u,v,w)$, u denotes the radial component of velocity so that the advective heat transport may be written

$$H_{adv}(\bar{r};\phi,z,t) = \int_{\phi_0}^{\phi_1}\int_{z_0}^{z_1} \rho(\bar{r};\phi,z,t)C_p(\bar{r};\phi,z,t)u(\bar{r};\phi,z,t)T(\bar{r};\phi,z,t)dz\bar{r}d\phi. \qquad (3.2)$$

Equation (3.2) is to be integrated between

$$\phi_0 = -(\pi-\epsilon)\ ,\ \phi_1 = \pi-\epsilon\ ,\ z_0 = -\frac{d}{2} + a(\bar{r};\phi)\ ,\ z_1 = \frac{d}{2}, \qquad (3.3)$$

where 2ϵ is the angular thickness of the barrier. When the base of the annulus is flat $a(\bar{r};\phi) = 0$, but $a(\bar{r};\phi) \neq 0$ for the experiments with sloping bases which are described in chapter 6.

Assuming the density and specific heat of the fluid to be constant:

$$\rho(\bar{r};\phi,z,t) \approx \bar{\rho}, \text{ and } C_p(\bar{r};\phi,z,t) \approx \bar{C}_p.$$

The overbar denotes the spatial average over the fluid, $\bar{(\ )} = \int(\ )dr\bar{r}d\phi dz[\int dr\bar{r}d\phi dz]^{-1}$. The values for $\bar{\rho}$ and $\bar{C}_p$ were taken to be the fluid density as measured in the laboratory at $20°C$, and the specific heat capacity of a water - glycerol solution of the appropriate density at $20°C$.

The temperature may be written

$$T(\bar{r};\phi,z,t) = \frac{\Delta T_\phi(\bar{r},z=0;t)}{2\pi}\phi + \frac{\Delta T_z(\bar{r},\phi=0;t)}{d}z + T'(\bar{r};\phi,z,t) + \bar{T}, \qquad (3.4)$$

where it should be noted that subscripts are not (and shall not be) used to represent derivatives. By definition $\Delta T_\phi(\bar{r},z=0;t)$ and $\Delta T_z(\bar{r},\phi=0;t)$ are

independent of ϕ and z, though not of t. ΔT_ϕ and ΔT_z have been formulated so that they correspond to the (potentially) measurable quantities of the azimuthal and vertical temperature differences in the fluid. It should be noted that equation (3.4) is formally correct because $T'(\bar{r};\phi,z,t)$ is a completely general function of ϕ, z and t. However the first two terms (linear in ϕ and z) have been chosen because they represent a useful approximation to the temperature in the analysis which follows. Ideally $\bar{T}$ should be defined in the same way as $\bar{\rho}$ above, however experimental constraints meant that in practice the quantity

$$\frac{\int T(\bar{r}, z=0;\phi,t)\bar{r}d\phi}{\int \bar{r}d\phi}$$

was used to calculate $\bar{T}$ when its value was required.

A further simplification is made by using

$$T'(\bar{r};\phi,z,t) \approx T'(\bar{r}, z=0;\phi,t). \tag{3.5}$$

This is done because the thermocouple ring data gives $T(\bar{r}, z=0;\phi,t)$ so while there is no prospect of being able to calculate any z dependence in T' it might be possible to calculate the ϕ dependence. A further consideration is that the 'kinks' that appear in the thermocouple ring data (e.g. see *Figure 3.9 (a)*) show that there are at least non-linearities in the ϕ dependence of T'. Using the approximations above equation (3.2) may be rewritten

$$H_{adv}(\bar{r};\phi,z,t) = \bar{\rho}\bar{C}_p \int_{\phi_0}^{\phi_1}\int_{z_0}^{z_1} u(\bar{r};\phi,z,t)T(\bar{r};\phi,z,t)dz\bar{r}d\phi. \tag{3.6}$$

It can be seen by comparison with equation (3.4) that equation (3.6) contains the term

$$\bar{\rho}\bar{C}_p \int_{\phi_0}^{\phi_1}\int_{z_0}^{z_1} u(\bar{r};\phi,z,t)\bar{T}dz\bar{r}d\phi.$$

However because the fluid is assumed to be incompressible, and the walls of the annulus are non-porous, the net flux of fluid through the surface at $r=\bar{r}$ must

be zero. Hence

$$\bar{\rho}\bar{C}_p \int_{\phi_0}^{\phi_1}\int_{z_0}^{z_1} u(\bar{r};\phi,z,t)\bar{T}dz\bar{r}d\phi = \bar{\rho}\bar{C}_p\bar{T}\int_{\phi_0}^{\phi_1}\int_{z_0}^{z_1} u(\bar{r};\phi,z,t)dz\bar{r}d\phi = 0.$$

Hence the advective heat transport may be written

$$H_{adv}(\bar{r};\phi,z,t) = \bar{\rho}\bar{C}_p \int_{\phi_0}^{\phi_1}\int_{z_0}^{z_1} u(\bar{r};\phi,z,t)\left[T(\bar{r};\phi,z,t)-\bar{T}\right]dz\bar{r}d\phi. \tag{3.7}$$

If the flow is split into the two circulations suggested in section 3.2.1 and illustrated in *Figure 3.12*, then $u(\bar{r};\phi,z,t)$ may be written

$$u(\bar{r};\phi,z,t) = u_\eta(\bar{r};z,t) + u_\zeta(\bar{r};\phi,t) + u'(\bar{r};\phi,z,t), \tag{3.8}$$

where $u_\eta(\bar{r};z,t)$ represents the radial velocity at $r=\bar{r}$ due to the η-circulation and $u_\zeta(\bar{r};\phi,t)$ is the radial velocity due to the ζ-circulation. $u'(\bar{r};\phi,z,t)$ represents any other flows that may be present in the fluid, and in particular will include the eddies seen at higher values of Ω. Since $u'(\bar{r};\phi,z,t)$ is a perfectly general function of ϕ, z and t, equation (3.8) is formally correct. Thus $H_{adv}(\bar{r};\phi,z,t)$ may be written as

$$H_{adv}(\bar{r};\phi,z,t) = H_\eta(\bar{r};\phi,z,t) + H_\zeta(\bar{r};\phi,z,t) + H'(\bar{r};\phi,z,t), \tag{3.9}$$

where $H_\eta(\bar{r};\phi,z,t)$ is the heat advected by the η-circulation, $H_\zeta(\bar{r};\phi,z,t)$ is the heat advected by the ζ-circulation and $H'(\bar{r};\phi,z,t)$ is the heat advected by any other processes, including the eddies. Thus H_η, H_ζ and H' may be defined as:

$$H_\eta(\bar{r};\phi,z,t) \equiv \bar{\rho}\bar{C}_p \int_{\phi_0}^{\phi_1}\int_{z_0}^{z_1} u_\eta(\bar{r};z,t)\left[T(\bar{r};\phi,z,t)-\bar{T}\right]dz\bar{r}d\phi, \tag{3.10}$$

$$H_\zeta(\bar{r};\phi,z,t) \equiv \bar{\rho}\bar{C}_p \int_{\phi_0}^{\phi_1}\int_{z_0}^{z_1} u_\zeta(\bar{r};\phi,t)\left[T(\bar{r};\phi,z,t)-\bar{T}\right]dz\bar{r}d\phi, \tag{3.11}$$

and

$$H'(\bar{r};\phi,z,t) \equiv \bar{\rho}\bar{C}_p \int_{\phi_0}^{\phi_1}\int_{z_0}^{z_1} u'(\bar{r};\phi,z,t)\left[T(\bar{r};\phi,z,t)-\bar{T}\right]dz\bar{r}d\phi. \tag{3.12}$$

Each of these terms is discussed below. In the case of the η-circulation it has been possible to propose a mechanism, so that an expression for $u_\eta(\bar{r};z,t)$ can be derived. For H_ζ and H' this has proved difficult, and only their advective heat transport contributions are discussed in this chapter.

3.2.3 Suggested mechanism for the η-circulation.

Following Hide's suggestion, as reported by *Bowden (1961)* (see also §1.3.2). The approximately linear dependence of u on z shown in *Figure 3.5* and the appearance of a temperature drop across the barrier suggest that $u_\eta(\bar{r};z,t)$ may be governed by a balance between the Coriolis force and an azimuthal pressure gradient supported by the barrier. The scaling arguments of §1.2.2 (*Table 1.1 (b)*), suggest that there could be reasonable geostrophic balance in the ϕ-direction down to the smallest rotation rates ($\Omega \sim 0.1\ rad.sec^{-1}$). Thus the part of the so-called 'Thermal Wind' equation (1.11) which describes $\partial u/\partial z$ might be expected to give a good approximation for $\partial u_\eta/\partial z$. Thus:

$$\frac{\partial u}{\partial z}(\bar{r};\phi,z,t) \approx -\frac{g\alpha}{2\Omega\bar{r}}\frac{\partial T}{\partial \phi}(\bar{r};\phi,z,t).$$

Integration then gives

$$|u(\bar{r};\phi,z,t)| \approx \frac{g\alpha}{2\Omega\bar{r}}\int_z \frac{\partial T}{\partial \phi}(\bar{r};\phi,z,t)dz + u_c(\bar{r};\phi,t),$$

where $u_c(\bar{r};\phi,t)$ is the function of integration. Substituting for $T(\bar{r};\phi,z,t)$ from equation (3.4), using (3.5), and expressing u_c as the sum of $u_0(\bar{r};\phi,t)$ (which is linear in ϕ) and $u_1(\bar{r};\phi,t)$ (which is a completely general function of ϕ) means that $u(\bar{r};\phi,z,t)$ can be rewritten

$$\begin{aligned}|u(\bar{r};\phi,z,t)| \;\approx\; & \frac{g\alpha}{2\Omega\bar{r}}\int_z \frac{\Delta T_\phi(\bar{r},z=0;t)}{2\pi}dz + u_0(\bar{r};\phi,t) \\ & + \left[\frac{g\alpha}{2\Omega\bar{r}}\int_z \frac{\partial T'}{\partial\phi}(\bar{r},z=0;\phi,t)dz + u_1(\bar{r};\phi,t)\right]. \qquad (3.13)\end{aligned}$$

Comparison with equation (3.8), noticing that the first term on the right hand side of (3.13) is a function of $(\bar{r};z,t)$ shows that

$$|u_\eta(\bar{r};z,t)| \approx \frac{g\alpha}{2\Omega\bar{r}}\int_z \frac{\Delta T_\phi}{2\pi}(\bar{r},z=0;t)dz. \qquad (3.14)$$

Similarly the second term is a function of $(\bar{r};\phi,t)$, so that $u_0(\bar{r};\phi,t)$ is $u_\zeta(\bar{r};\phi,t)$, while the final term (in square brackets) expresses $u'(\bar{r};\phi,z,t)$.

Now $H_\eta(\bar{r};\phi,z,t)$ can be obtained by substituting equations (3.14) and (3.4) into (3.10). Integration over z then gives:

$$\begin{aligned}H_\eta(\bar{r};\phi,z,t) \;\approx\; & \frac{\bar{\rho}\bar{C}_p g\alpha\Delta T_\phi}{4\Omega\pi}\int_{\phi_0}^{\phi_1}\left[\frac{\Delta T_\phi(\bar{r},z=0;t)}{4\pi}\phi z^2\right. \\ & \left. + \frac{\Delta T_z(\bar{r},\phi=0;t)}{3d}z^3 + \frac{T'(\bar{r},z=0;\phi,t)}{2}z^2\right]_{z_0}^{z_1} d\phi.\end{aligned}$$

The limits on z are given in equation (3.3). Thus

$$\begin{aligned}& H_\eta(\bar{r};\phi,z,t) \approx \\ & \frac{\bar{\rho}\bar{C}_p g\alpha\Delta T_\phi(\bar{r},z=0;t)}{4\Omega\pi}\int_{\phi_0}^{\phi_1}\left\{\left[\frac{\Delta T_z(\bar{r},\phi=0;t)d^2}{12}\right]\right. \\ & + \left[\frac{\Delta T_\phi(\bar{r},z=0;t)}{4\pi}\phi a(d-a) + \frac{\Delta T_z(\bar{r},\phi=0;t)}{3d}\left(-\frac{3ad^2}{4}+\frac{3a^2d}{2}-a^3\right)\right. \\ & \left.\left. + \frac{T'(\bar{r},z=0;\phi,t)}{2}a(d-a)\right]\right\}d\phi, \qquad (3.15)\end{aligned}$$

where $a = a(\bar{r};\phi)$. Equation (3.15) is required later, with $a(\bar{r};\phi) \neq 0$ when the results with sloping bases are analysed in chapter 6; however when the base is flat $a(\bar{r};\phi) = 0$, the second term in the square brackets vanishes, and

$$H_\eta(\bar{r},a=0;t) \approx \frac{\bar{\rho}\bar{C}_p g\alpha\Delta T_\phi(\bar{r},z=0;t)\Delta T_z(\bar{r},\phi=0;t)d^2(\pi-\epsilon)}{24\Omega\pi}.$$

Since the half-angular thickness of the barrier $\epsilon \ll \pi$ it can be neglected, also since there was no data available for $\Delta T_z(\bar{r},\phi=0;t)$, the approximation was made that $\Delta T_z \approx \Delta T$. Further, putting $\Delta T_\phi = \Delta T_B$ means that $H_\eta(\bar{r},a=0;t)$ can now be expressed only in terms of experimental parameters and fluid properties:

$$H_\eta(\bar{r},a=0;t) \approx \frac{\bar{\rho}\bar{C}_p g\alpha\Delta T_B\Delta T d^2}{24\Omega}. \qquad (3.16)$$

If it is possible to find a region of parameter space where the η-circulation is the primary cause of heat advection in the system, then it should be possible to test the result of equation (3.16) explicitly.

3.2.4 Testing the theory for the η-circulation.

If heat advection by eddies forms the main contribution to $H'(\bar{r};\phi,z,t)$, then at values of Ω where no eddies form ($\Omega \lesssim 1.2\ rad.sec^{-1}$), $H'(\bar{r};\phi,z,t) \approx 0$. Also *Figures 3.2 - 3.4, 3.6, 3.7* suggest that the ζ-circulation is weakest at small Ω. Hence it is possible to make the hypothesis that at small Ω, the η-circulation dominates the heat advection, so that equation (3.9) becomes

$$H_{adv}(\bar{r};\phi,z,t) \approx H_{\eta}(\bar{r},a=0;t).$$

If this is the case, then by (3.16),

$$H_{adv}(\bar{r},a=0;t) \approx \frac{\bar{\rho}\bar{C}_p g\alpha\Delta T_B \Delta T d^2}{24\Omega}.$$

Hence it is possible to define a quantity A_* as

$$A_*^{-1} \equiv \frac{24\Omega H_{adv}(\bar{r},a=0;t)}{\bar{\rho}\bar{C}_p g\alpha\Delta T_B\Delta T d^2}, \qquad (3.17)$$

where it is expected that $A_* \sim 1$ at low rotation rates. *Figure 3.13* shows plots of A_*^{-1} against Ω for the two values of ΔT used in the experiments. It can be seen that for $\Omega \lesssim 3.0\ rad.sec^{-1}$, when $\Delta T = 4\ K$, $A_*^{-1} \approx 1.15$ giving $A_* \approx 0.9$. A similar value is found for $\Delta T = 10\ K$, but over a larger range of Ω. Only at quite large rotation rates in *Figure 3.13 (a)* does A_*^{-1} deviate significantly from unity, which is to be expected as the heat advection from the ζ-circulation and the eddies becomes more important at higher Ω. The interpretation of A_*^{-1} can be assisted by noticing that by substituting (3.16) into (3.17), $A_*^{-1} \approx H_{adv}/H_{\eta}$,

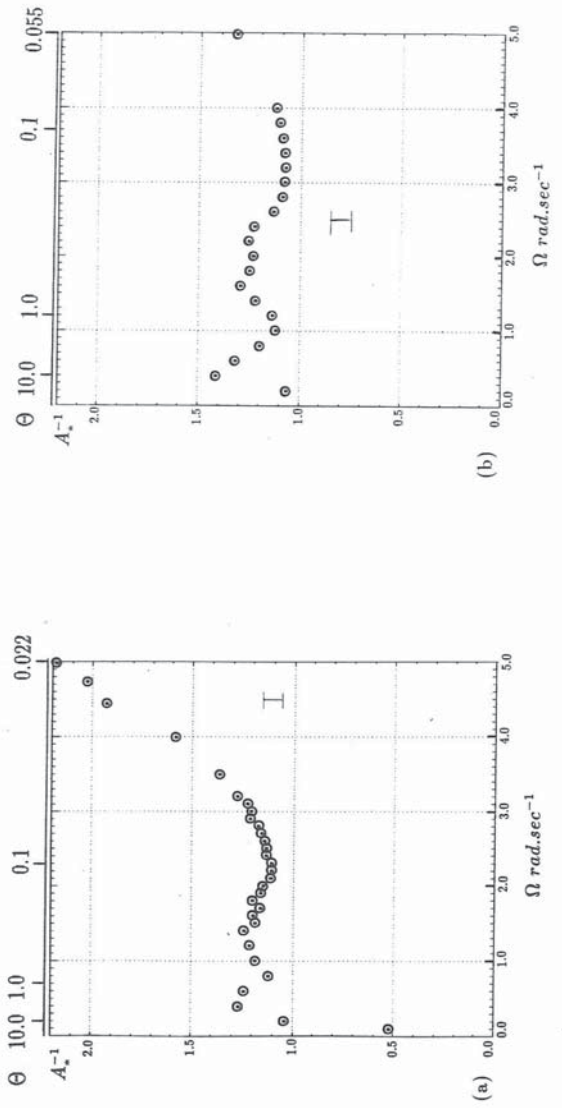

FIGURE 3.13: Plots of the dimensionless quantity $A_*^{-1} = 24\Omega H(\rho C_p g\alpha\ \Delta T d^2 \Delta T_B)^{-1}$ against Ω for the system with a full thermally insulating barrier and depth $d = 140\ mm$. (a) $\Delta T = 4\ K$, A_*^{-1} appears to be of order unity for Ω less than about 3.0 $rad.sec^{-1}$ and then increases fairly linearly with Ω at higher rotation rates. (b) $\Delta T = 10\ K$, A_*^{-1} remains of order unity over the range of Ω shown.

this proves helpful in later discussions.

This result agrees closely with the hypothesis made above, namely that only the η-circulation makes a significant contribution to the heat advection at low rotation rates ($\Omega \lesssim 3.0\ rad.sec^{-1}$), and provides strong evidence that equation (3.16) correctly describes heat advection by the η-circulation.

The simple linear dependence of A_*^{-1} on Ω for higher rotation rates in *Figure 3.13 (a)* allows A_* to be expressed empirically as

$$A_* = A.\mathrm{Min}(1, R_D/R), \tag{3.18}$$

where the function 'Min(x, y)' is defined as the smaller of the two quantities x and y, and

$$R_D \equiv \frac{\sqrt{g\alpha\Delta T d}}{2\Omega}. \tag{3.19}$$

R_D can be regarded as an estimate of the Rossby radius of deformation for the fluid. In this case equation (3.17) can be written

$$Y(\bar{r}, a = 0; \Omega, t) \approx \frac{24\Omega H_{adv}(\bar{r}, a = 0; t)\mathrm{Min}(1, R_D/R)}{\bar{\rho}\bar{C}_p g\alpha\Delta T d^2}.A, \tag{3.20}$$

where it is to be expected that $Y \approx \Delta T_B$. *Figure 3.14* shows plots of $Y(\bar{r}, a = 0; \Omega, t)$ against ΔT_B, where $A \sim 1$ and $R \sim 1\ cm$. It can be seen that there is almost complete agreement to within the accuracy of the error bars. Thus $Y(\bar{r}, a = 0; \Omega, t)$ in equation (3.20) provides a very good estimate of ΔT_B if H_{adv} is known, or vice - versa.

A further test for the mechanism for the η-circulation can be seen from equation (3.14). By substituting ΔT_B for ΔT_ϕ in (3.14) and considering *Figure 3.10* it can be seen that while $\Delta T_B \propto \Omega$, equation (3.14) predicts that $u_\eta(\bar{r}; z, t)$ should be independent of Ω; up to about 3.0 $rad.sec^{-1}$ in the $\Delta T = 4\ K$ case, and for a greater range when $\Delta T = 10\ K$. This observation is supported by *Figure 3.5* where this does indeed appear to be the case. *Table 3.3* shows the maximum

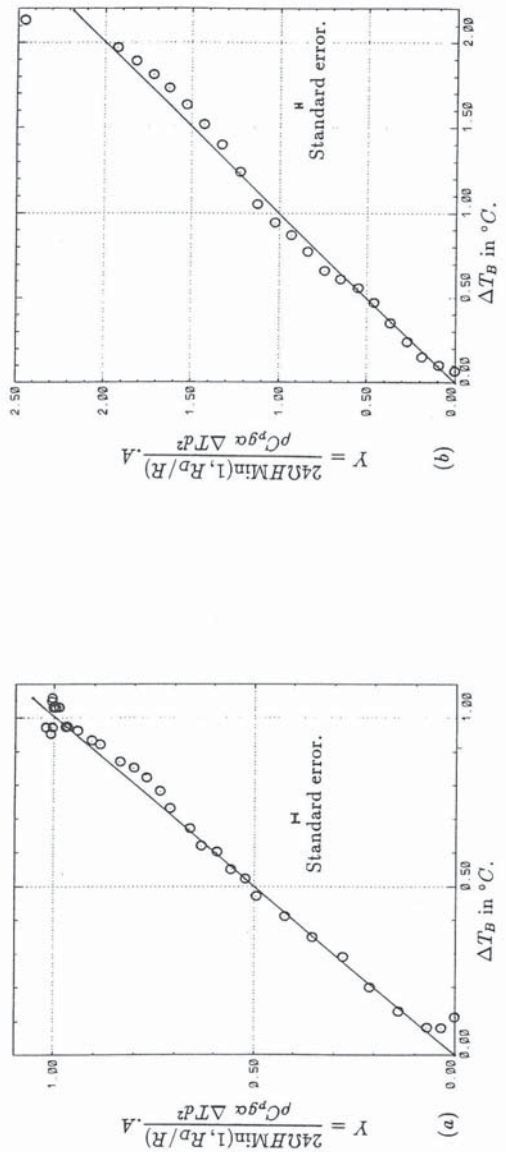

FIGURE 3.14: Plots of the quantity Y against experimental measurements of ΔT_B, for the system with a full thermally insulating barrier and depth, $d = 140\ mm$. In both cases the results fall quite closely onto a straight line of gradient unity, indicating that $\Delta T_B \approx Y$ over the range shown. For (a) $\Delta T = 4\ K$, $A = 0.85$, $R = 0.71\ cm$ and (b) $\Delta T = 10\ K$, $A = 0.87$, $R \leq 0.64\ cm$.

positive and negative values of u against Ω. These results are plotted in *Figure 3.15*, and u does appear to be constant to the accuracy of the error bars, at least up to $\Omega = 3.0\ rad.sec^{-1}$ and possibly beyond. This provides a further piece of evidence that (3.14) correctly describes $u_\eta(\bar{r}; z, t)$.

	$\Delta T \approx 4\ K$			—		$\Delta T \approx 10\ K$		
Run No	Ω $rad.sec^{-1}$	Max $u > 0$ $mm.sec^{-1}$	Max $u < 0$ $mm.sec^{-1}$	Error in u $mm.sec^{-1}$	Run No	Ω $rad.sec^{-1}$	Max $u > 0$ $mm.sec^{-1}$	Max $u < 0$ $mm.sec^{-1}$
210	0.489	0.18	-0.20	0.09	227	0.500	0.20	-0.25
211	0.195	0.14	-0.21	0.09	228	0.200	0.16	-0.24
212	0.391	0.13	-0.20	0.09	229	0.400	0.20	-0.26
213	0.589	0.16	-0.15	0.09	230	0.599	0.18	-0.25
215	0.980	0.18	-0.18	0.09	231	0.799	0.22	-0.27
216	1.176	0.16	-0.19	0.09	232	1.000	0.18	-0.27
217	1.372	0.19	-0.18	0.09	233	1.196	0.25	-0.28
218	1.569	0.16	-0.19	0.09	234	1.402	0.23	-0.28
219	1.665	0.18	-0.18	0.09	236	1.000	0.21	-0.27
221	2.000	0.16	-0.16	0.09	237	1.196	0.23	-0.26
222	2.500	0.17	-0.18	0.09	238	1.697	0.24	-0.24
223	2.000	0.16	-0.15	0.09	239	2.000	0.23	-0.23
224	1.999	0.15	-0.15	0.09	240	2.500	0.27	-0.23
225	3.503	0.10	-0.15	0.09	241	3.003	0.22	-0.24
226	3.002	0.17	-0.16	0.09	242	3.504	0.18	-0.25

TABLE 3.3: Measurements of the maximum positive, and maximum negative values of u, measured during the experiments with a full, thermally insulating barrier.

3.2.5 Heat advection by the ζ-circulation.

Equation (3.11) gives the heat advection by the ζ-circulation, $H_\zeta(\bar{r}; \phi, z, t)$. However without knowing the mechanism for that circulation it is impossible to write an equation to describe $u_\zeta(\bar{r}; \phi, t)$. $H_\zeta(\bar{r}; \phi, z, t)$ can still be estimated from experimental measurements of velocity. If $u_\zeta(\bar{r}; \phi, t)$ is assumed to have a linear dependence on ϕ, then

$$u_\zeta(\bar{r}; \phi, t) = \frac{\Delta u_\phi(\bar{r}, z = 0; t)}{2\pi}\phi,$$

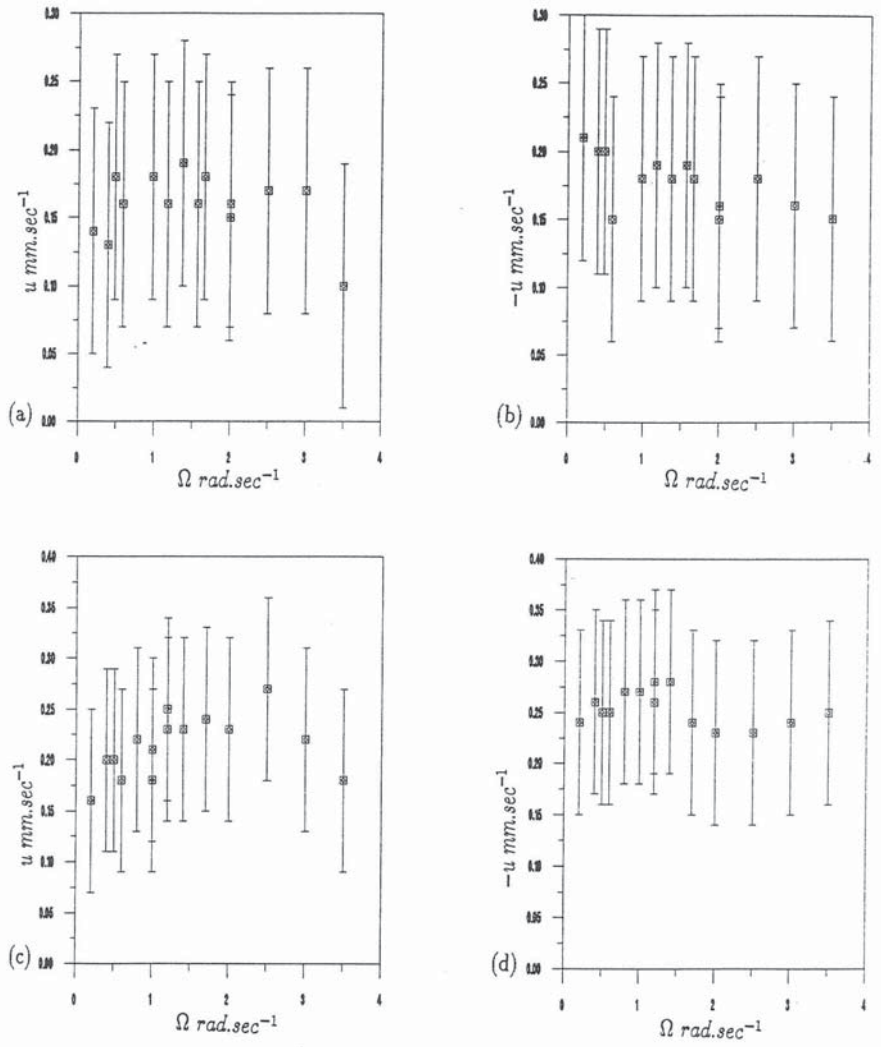

FIGURE 3.15: Plots of (a), (c) maximum positive u against Ω, (b), (d) maximum negative u against Ω, for (a), (b) $\Delta T = 4\ K$ and (c), (d) $\Delta T = 10\ K$, using the velocity results given in Table 3.3. The results all show that, to the accuracy of the error bars, u is constant with Ω. This result is consistent with equation (3.14) and the mechanism proposed for the η-circulation in §3.2.3.

so that equation (3.11) can be written

$$H_\zeta(\bar{r};\phi,z,t) \approx \bar{\rho}\bar{C}_p \int_{\phi_0}^{\phi_1}\int_{z_0}^{z_1} \frac{\Delta u_\phi(\bar{r},z=0;t)}{2\pi}\phi\left[T(\bar{r};\phi,z,t)-\bar{T}\right]dz\bar{r}d\phi.$$

Integration over z leads to

$$\begin{aligned} H_\zeta(\bar{r};\phi,z,t) \approx\ & \frac{\bar{\rho}\bar{C}_p\Delta u_\phi(\bar{r},z=0;t)}{2\pi}\int_{\phi_0}^{\phi_1}\left\{\left[\frac{\Delta T_\phi(\bar{r},z=0;t)}{2\pi}\phi^2 d + T'(\bar{r},z=0;\phi,t)\phi d\right]\right. \\ & +a\left[-\frac{\Delta T_\phi(\bar{r},z=0;t)}{2\pi}\phi^2 + \frac{\Delta T_z(\bar{r},\phi=0;t)}{2d}\phi(d-a)\right. \\ & \left.\left.-T'(\bar{r},z=0;\phi,t)\phi\right]\right\}\bar{r}d\phi, \end{aligned} \tag{3.21}$$

where $a = a(\bar{r};\phi)$. In the flat base case $a(\bar{r};\phi) = 0$ and the second term in square brackets vanishes, so that integration yields

$$\begin{aligned} & H_\zeta(\bar{r},a=0;\phi,t) \approx \\ & \frac{\bar{\rho}\bar{C}_p\Delta u_\phi(\bar{r},z=0;t)\bar{r}d}{2\pi}\left[\frac{\Delta T_\phi(\bar{r},z=0;t)\pi^2}{3} + \int_{\phi_0}^{\phi_1} T'(\bar{r},z=0;\phi,t)\phi d\phi\right], \end{aligned} \tag{3.22}$$

where the approximation that the angular half-width of the barrier, $\epsilon \ll \pi$ has again been made. As before put $\Delta T_\phi \approx \Delta T_B$, and $\int T'(\bar{r},z=0;\phi,t)\phi d\phi$ can be calculated from the thermocouple ring measurements, $T(\bar{r},z=0;\phi,t)$ using a simple numerical scheme [1]. Δu_ϕ must be estimated from experimental velocity measurements. *Table 3.4* gives the maximum positive and negative values of v from the experiments.

As the measurements of v were perpendicular to the flow in the η-circulation, they can only arise from the ζ-circulation. *Figure 3.16* shows plots of v against Ω, from where it can be seen that

$$|v| \approx 0.02\Omega\ cm.sec^{-1} \ \text{ at } \Delta T \approx 4\ K,$$

[1] $\int T'\phi d\phi$ was calculated as follows: $\int_{\phi_0}^{\phi_1} T'\phi d\phi \approx \Sigma_{i=1}^{32} T'_i\phi_i\delta\phi$, where $T'_i = T'(\bar{r},z=0;\phi_i,t)$, $\phi_i = 2\pi(i-1)/32 + 2\pi/64$, $\delta\phi = 2\pi/32$ and i is the thermocouple ring number.

	$\Delta T \approx 4\ K$			—		$\Delta T \approx 10\ K$		
Run No	Ω $rad.sec^{-1}$	Max $v>0$ $mm.sec^{-1}$	Max $v<0$ $mm.sec^{-1}$	Error in v $mm.sec^{-1}$	Run No	Ω $rad.sec^{-1}$	Max $v>0$ $mm.sec^{-1}$	Max $v<0$ $mm.sec^{-1}$
210	0.489	0.28	-0.16	0.09	227	0.500	0.43	-0.15
211	0.195	0.20	-0.11	0.09	228	0.200	0.26	-0.09
212	0.391	0.27	-0.17	0.09	229	0.400	0.42	-0.11
213	0.589	0.26	-0.19	0.09	230	0.599	0.45	-0.18
215	0.980	0.37	-0.36	0.09	231	0.799	0.48	-0.24
216	1.176	0.27	-0.36	0.09	232	1.000	0.48	-0.28
217	1.372	0.38	-0.41	0.09	233	1.196	0.45	-0.34
218	1.569	0.36	-0.35	0.09	234	1.402	0.59	-0.39
219	1.665	0.41	-0.43	0.09	235	1.598	0.68	-0.55
221	2.000	0.44	-0.40	0.09	236	1.000	0.48	-0.29
222	2.500	0.44	-0.50	0.09	237	1.196	0.48	-0.32
223	2.000	0.39	-0.35	0.09	238	1.697	0.66	-0.56
224	1.999	0.43	-0.37	0.09	239	2.000	0.54	-0.65
225	3.503	0.76	-0.77	0.09	240	2.500	0.51	-0.53
226	3.002	0.58	-0.65	0.09	241	3.003	0.84	-0.75
-	-	-	-	0.09	242	3.504	1.00	-0.90

TABLE 3.4: Measurements of the maximum positive, and maximum negative values of the azimuthal component of velocity, for the experiments with a flat base and a fully blocking thermally insulating barrier.

and

$$|v| \approx 0.03\Omega\ cm.sec^{-1} \ \text{ at } \Delta T \approx 10\ K.$$

Using the equation for incompressible flow (1.2), and making use of the fact that $w \ll u, v$;

$$\frac{1}{r}\frac{\partial(ru)}{\partial r} + \frac{1}{r}.\frac{\partial v}{\partial\phi} \approx 0\ ,\ \Rightarrow\ u \approx -\frac{1}{r}\int\frac{\partial v}{\partial\phi}dr + \frac{u_c(\phi,z,t)}{r}.$$

This suggests that

$$\Delta u_\phi(\Delta T \approx 4\ K) \approx \frac{1}{\bar{r}}.\frac{0.02\Omega}{2\pi}.(b-a) = \frac{0.11\Omega}{2\pi\bar{r}}.$$

and

$$\Delta u_\phi(\Delta T \approx 10\ K) \approx \frac{1}{\bar{r}}.\frac{0.03\Omega}{2\pi}.(b-a) = \frac{0.17\Omega}{2\pi\bar{r}}.$$

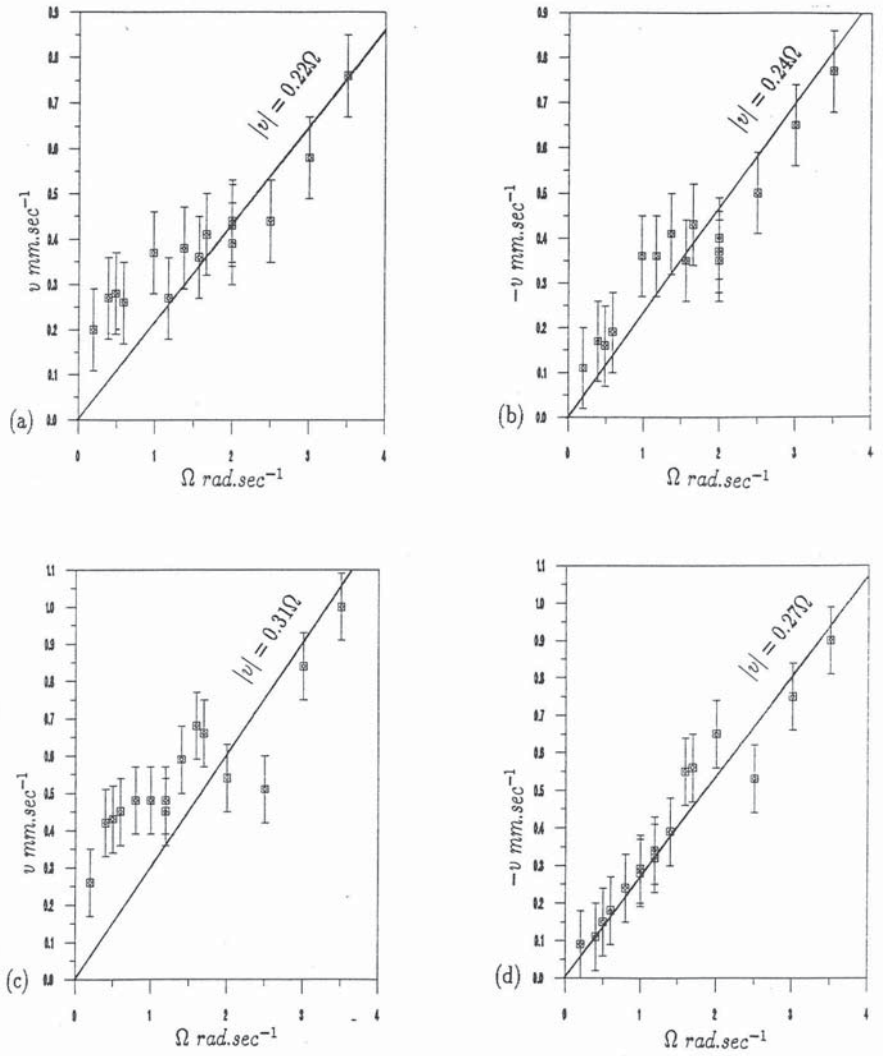

FIGURE 3.16: Plots of (a), (c) maximum positive v against Ω, (b), (d) maximum negative v against Ω, for (a), (b) $\Delta T = 4\ K$ and (c), (d) $\Delta T = 10\ K$, using the velocity results given in Table 3.4. Also plotted are solid lines showing (a), (b) $v = 0.2\Omega\ mm.sec^{-1}$, and (c), (d) $v = 0.3\Omega\ mm.sec^{-1}$.

Thus equation (3.22) can be written

$$\begin{aligned} H_\zeta(\bar{r}, a=0, \Delta T \approx 4\ K; \phi, t) &\approx \frac{0.11\bar{\rho}\bar{C}_p\Delta T_B\Omega d}{12} + \frac{0.11\bar{\rho}\bar{C}_p\Omega d}{4\pi^2}\int_{\phi_0}^{\phi_1} T'\phi d\phi, \\ H_\zeta(\bar{r}, a=0, \Delta T \approx 10\ K; \phi, t) &\approx \frac{0.17\bar{\rho}\bar{C}_p\Delta T_B\Omega d}{12} + \frac{0.17\bar{\rho}\bar{C}_p\Omega d}{4\pi^2}\int_{\phi_0}^{\phi_1} T'\phi d\phi. \end{aligned} \tag{3.23}$$

Estimates of the error in H_ζ were obtained by taking the steepest and shallowest slopes of the linear fit used to describe $|v|$ in *Figure 3.16*; these gave an error of 15% when $\Delta T \approx 4\ K$ and 17% for $\Delta T \approx 10\ K$. Though it should be noted that since the maximum positive and negative values of v have been used, equation (3.23) is more likely to be an over estimate of H_ζ than an under estimate. Values for $H_\zeta(\bar{r}, a=0; \phi, t)$ are plotted in *Figure 3.17*, along with the heat advection contributions of the η-circulation, and the total advective heat transport as measured by the experiments.

3.2.6 Heat advection by eddies.

The heat advection by the eddies is given by equation (3.12). As $u'(\bar{r}; \phi, z, t)$ could not be measured for $\Omega \gtrsim 3.0\ rad.sec^{-1}$, due to the limitations of the velocity measurement apparatus, the best that could be done was to estimate the order of magnitude of $H'(\bar{r}; \phi, z, t)$ when eddies were present. Another problem was that velocity and temperature measurements could not be made simultaneously, so that it was not possible to correlate the velocity and temperature measurements for the eddies. *Figure 3.7 (c)* can be used to estimate the radial velocity shear with ϕ of an eddy as $\Delta u_B \sim 0.84\ mm.sec^{-1}$ at $\Omega = 3.0\ rad.sec^{-1}$ and $\Delta T \approx 10\ K$. At the same values of Ω and ΔT temperature measurements gave the difference between the maximum and minimum values of T', $\Delta T'$ as $0.530\ K$ [2]. Also as the

[2] $\Delta T'$ was calculated as follows: $\Delta T' = T'_{max} - T'_{min}$, where T'_{max} was the largest value of T' calculated from the thermocouple ring data, and T'_{min} the smallest value. From equation (3.4) $T'(\bar{r}, z=0; \phi, t) \approx T(\bar{r}, z=0; \phi, t) - \Delta T_B\phi/2\pi - \bar{T}$, using $\Delta T_\phi \approx \Delta T_B$.

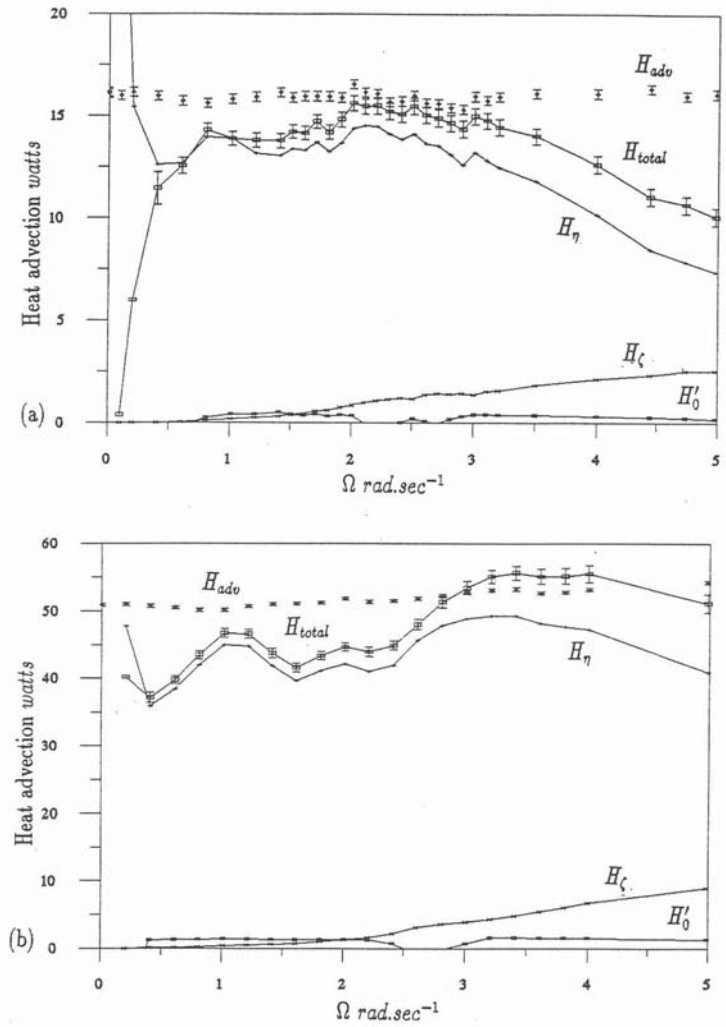

FIGURE 3.17: Plots showing the heat transport contributions for the insulating barrier with the flat base. Heat transport contributions have been calculated for; the η-circulation, H_η, using equation (3.16); the ζ-circulation, H_ζ, using equation (3.23); and H_0', using equation (3.25). $H_{total} = H_\eta + H_\zeta + H_0'$. Experimental measurements of the advective heat transport, H_{adv} are shown for comparison. (a) $\Delta T \approx 4\ K$, (b) $\Delta T \approx 10\ K$. The lines serve only as a guide to the eye.

eddy in *Figure 3.7 (c)* only occupies about one-fifth of the azimuth, $\delta\phi \sim 2\pi/5$. So that the *maximum* amount of heat the eddy could carry (if u' and T' were suitably correlated) would be

$$H'(\bar{r};\phi,z,t) \sim \bar{\rho}\bar{C}_p \Delta u_B \Delta T' \bar{r} d \frac{2\pi}{5} = 17\ watts.$$

Comparison with *Figure 3.17* indicates that the eddy was not carrying much heat, suggesting that u' and T' were not well correlated in this case. However the calculation does indicate that eddies are quite capable of carrying significant amounts of heat. The fact that eddies are capable of carrying significant amounts of heat does suggest that the eddies might be responsible for the increase in Nu seen in *Figure 3.11 (b)*, which does seem to occur for $\Omega \gtrsim 1.6\ rad.sec^{-1}$, which is the same as the transition for the onset of the eddies at $\Delta T \approx 10\ K$.

In an attempt to explore the heat advection by eddies a little further, equation (3.13) suggests that

$$u'(\bar{r};\phi,z,t) \approx \frac{g\alpha}{2\Omega\bar{r}} \int_z \frac{\partial T'}{\partial \phi}(\bar{r}, z=0;\phi,t)dz + u_1(\bar{r};\phi,t),$$

where $u_1(\bar{r};\phi,t)$ is non-linear in ϕ. $H'(\bar{r};\phi,z,t)$ is given by equation (3.12). Though the mechanism for $u_1(\bar{r};\phi,t)$ remains unknown, it is possible to write

$$H'(\bar{r};\phi,z,t) = H_0'(\bar{r};\phi,z,t) + H_1'(\bar{r};\phi,z,t)$$

where

$$H_0'(\bar{r};\phi,z,t) \approx \bar{\rho}\bar{C}_p \int_{\phi_0}^{\phi_1} \int_{z_0}^{z_1} \frac{g\alpha}{2\Omega\bar{r}} \int_z \frac{\partial T'}{\partial \phi}(\bar{r}, z=0;\phi,t)dz \left[T(\bar{r};\phi,z,t) - \bar{T}\right] dz \bar{r} d\phi.$$

Substitution from equation (3.4) for $T(\bar{r};\phi,z,t)$, and integration over ϕ using the limits given in (3.3) gives

$$H_0'(\bar{r};\phi,z,t) \approx \frac{\bar{\rho}\bar{C}_p g\alpha}{2\Omega}\int_{\phi_0}^{\phi_1}\left\{\frac{\partial T'}{\partial\phi}(\bar{r},z=0;\phi,t)\frac{\Delta T_z(\bar{r},\phi=0;t)d^2}{12}\right.$$
$$+\frac{\partial T'}{\partial\phi}(\bar{r},z=0;\phi,t)\left[\frac{\Delta T_\phi(\bar{r},z=0;t)}{4\pi}\phi a(d-a)\right.$$
$$+\frac{\Delta T_z(\bar{r},\phi=0;t)}{3d}\left(-\frac{3ad^2}{4}+\frac{3a^2d}{2}-a^3\right)$$
$$\left.\left.+\frac{T'(\bar{r},z=0;\phi,t)}{2}a(d-a)\right]\right\}d\phi. \qquad (3.24)$$

When the annulus base is flat $a(\bar{r};\phi)=0$ and the term in square brackets vanishes, so that if $\Delta T_z \approx \Delta T$,

$$H_0'(\bar{r},a=0;\phi,t)\approx\frac{\bar{\rho}\bar{C}_p g\alpha\Delta T d^2}{24\Omega}\int_{\phi_0}^{\phi_1}\frac{\partial T'}{\partial\phi}(\bar{r},z=0;\phi,t)d\phi. \qquad (3.25)$$

Values of $H_0'(\bar{r},a=0;\phi,t)$ are plotted along with the other heat transport contributions in *Figure 3.17*[3]. It can be seen that the values of H_0' are rather small, and probably form only a tiny part of $H'(\bar{r};\phi,z,t)$. Equation (3.13) indicates that H_0' is the correction that should be applied to equation (3.14) to allow for variations in the strength of the η-circulation with ϕ due to non-linearities in $\partial T/\partial\phi$. As H_0' is so small, clearly such corrections are not very important. Consequently it appears that the important contributions to $u'(\bar{r};\phi,z,t)$ are made by $u_1(\bar{r};\phi,t)$, an idea which is supported by *Figure 3.7(c)* which shows $u(\bar{r};\phi,z,t)$ to have a much stronger dependence upon ϕ than on z in the region of the eddy.

3.3 Conclusions.

Section 3.1.3 gives a summary of the experimental results. It seems that the flow pattern observed may be regarded as a superposition of two circulations (see section 3.2.1), the η and ζ- circulations, and eddies at higher rotation rates.

Theory suggested that at $r=\bar{r}$ the r-component of the velocity for the η-circulation could be described by equation (3.14). Physically this represents a

[3] $\int\partial T'/\partial\phi d\phi$ was calculated as follows: $\int_{\phi_0}^{\phi_1}\partial T'/\partial\phi d\phi = T'(\phi_1)-T'(\phi_0)\approx T'_{32}-T'_1$, where T'_i is the value of T' at the i^{th} thermocouple.

balance between the Coriolis force and an azimuthal pressure gradient supported by the barrier. The pressure drop across the barrier is associated with the temperature drop ΔT_B. Heat advection by the η-circulation is described by equation (3.16). At values of Ω less than 3.0 $rad.sec^{-1}$ for $\Delta T = 4\ K$, and over a larger range when $\Delta T = 10\ K$ the heat advection of the η-circulation gives a good approximation to the heat advection measured in the experiments. This appears to correspond to the case when the ζ-circulation and the eddies transport little heat so that only the η-circulation contributes significantly to the heat advection by the fluid. In this range equation (3.16) provides a diagnostic equation which links the heat advection to ΔT_B through experimental parameters and fluid properties. Thus there appears to be strong evidence that suggests that the η-circulation is correctly parameterized by equations (3.14) and (3.16) and described by the physical mechanism described above.

Further, equations (3.18) - (3.20) provide a set of empirically based diagnostic equations which link the heat advection to ΔT_B in a similar fashion, over the whole range of Ω covered in the experiments.

While the mechanism for the ζ-circulation has not been revealed, velocity measurements have allowed its heat advection to be estimated by equation (3.23). Estimates of heat advection by eddies show that they may play a significant role in heat advection when present.

Figure 3.17 shows the heat advection contributions of the various processes described above. While these mechanisms do seem to account for the bulk of the measured heat advection, there are still regions where the discrepancy is greater than the error bars. At the very smallest values of Ω this may be because then geostrophic balance in the ϕ direction is no longer valid, so that equation (3.13) is no longer appropriate. At large values of Ω it seems possible that eddies will play an increasingly important role in heat advection. However a weakness in the

theory is that $\partial T/\partial\phi$ has been assumed to be independent of z, and ΔT_z has not been measured at all, this may also be the cause of the less good agreement at smaller values of Ω.

Despite these problems there is sufficient agreement between the theory and the measurements to suggest that the mechanisms keeping the heat advection close to its non-rotating value over the range of Ω appear to be as follows.

At low to medium rotation rates heat is advected mainly by the η-circulation, at a rate which is independent of Ω (according to equation (3.16)) so long as $\Delta T_B \propto \Omega$. The heat advection by the ζ-circulation is insignificant as ΔT_B is rather smaller than $\Delta T_z \approx \Delta T$ and because $u_\zeta(\bar{r};\phi,t)$ is small at small Ω. At higher values of Ω, the ζ- circulation plays an increasingly important role in heat advection, but it always transports less heat than the η-circulation. The contribution of the η-circulation begins to decrease once ΔT_B stops increasing with Ω (see *Figure 3.10*). Heat advection by the η and ζ-circulations is unable to account for the total heat advected by the fluid at all rotation rates according to the measurements. Because no other processes appear to be present in the fluid, and because eddies may be able to transport significant amounts of heat (as section 3.2.6 shows) it is *suggested* that the remainder of the heat may be transported by the eddies.

Figure 3.17 (a) shows that no significant heat advection is required of the eddies until $\Omega \sim 3.0\ rad.sec^{-1}$ at $\Delta T \approx 4\ K$ (i.e. when ΔT_B stops increasing with Ω), yet *Table 3.1* shows that eddies first appear at $\Omega \gtrsim 1.2\ rad.sec^{-1}$. However eddies cannot transport heat effectively until $T'(\bar{r}, z=0;\phi,t)$ becomes significant. *Figure 3.9 (a)* shows that even at $\Omega = 1.9\ rad.sec^{-1}$, T' is very small because the themocouple ring data, $T(\bar{r}, z=0;\phi,t)$ is still closely linear. The values of $\Delta T'$ calculated for $\Delta T \approx 4\ K$ plotted in *Figure 3.18* show that $\Delta T'$ increases rapidly between $\Omega \approx 2.5\ rad.sec^{-1}$ and $3.0\ rad.sec^{-1}$. This

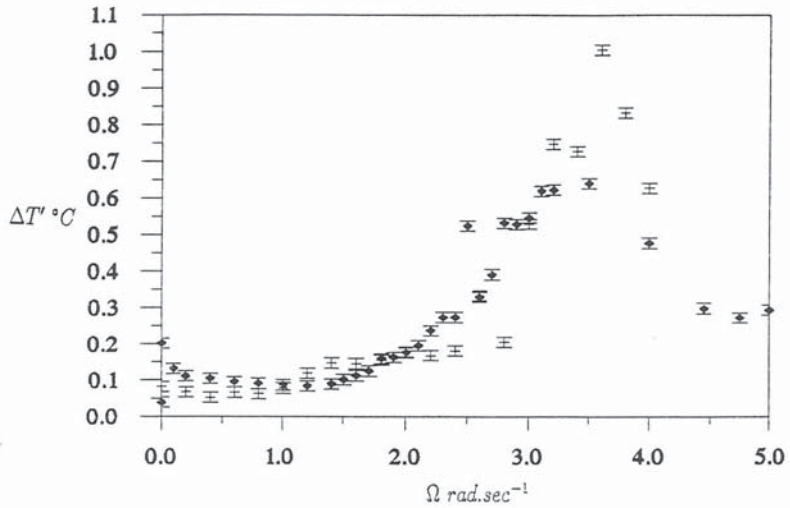

FIGURE 3.18: Plot of $\Delta T'$ against Ω for the results with the full insulating barrier. For $\Delta T'$ see §3.2.6. The solid diamonds are the $\Delta T \approx 4\ K$ results and the crosses, the 10 K results. $\Delta T'$ increases rapidly around $2.5\ rad.sec^{-1}$.

suggests that although the eddies first appear at much lower rotation rates, it is appearance of the 'kinks' in the themocouple ring data, $T(\bar{r}, z=0;\phi,t)$ (see *Figure 3.9 (a)*) which allows them to transport heat effectively. These 'kinks' start to appear at about the same values of Ω as those at which ΔT_B stops increasing with Ω.

Bowden (1961) found a relation for the heat transport in an unobstructed stationary annulus (1.19). Since there is no azimuthal motion in the annulus at $\Omega = 0$ (blocked or unblocked) his result should apply equally to the radial barrier measurements. The fact that Bowden's results were obtained in a system without a rigid lid is neglected. Using equation (1.14), Bowden's result

may be expressed,

$$\mathrm{Nu}(\Omega = 0) = (0.203 \pm 0.010)\mathrm{Ra}^{\frac{1}{4}}. \qquad (3.26)$$

Table 3.5 shows Bowden's results compared with the measurements of Nu when $\Omega = 0$ from *Table 3.2*. It can be seen that there is excellent agreement with equation (3.26).

Run No	ΔT °C	Nu	$0.203\mathrm{Ra}^{1/4}$	$\pm 0.010\mathrm{Ra}^{1/4}$
4U	4.02	11.14	10.94	±0.54
7R	4.05	11.10	10.96	±0.54
8M	10.01	13.88	13.74	±0.68

TABLE 3.5: Values of Nu at $\Omega = 0$ for the measurements made with a fully blocking thermally insulating radial barrier, compared with equation (3.26).

3.4 Further investigations.

The measurements described in this chapter have only been able to partially investigate the fluid motions and the heat transport measurements seen in the experiments. A list of further investigations involving each of the processes (the two circulations and the eddies) is given below. These investigations are explored in later chapters of this thesis.

The η-circulation is described by equations (3.14) and (3.16). If these equations are correct then they predict that if $\Delta T_B = 0$, then $u_\eta(\bar{r}; z, t) = 0$ also, and the η-circulation is unable to carry any heat. To attempt to test this, a series of measurements were made with a thermally conducting barrier, made out of a thin sheet of copper, which could have the effect of 'short- circuiting' ΔT_B. The results of these investigations are reported in Chapter 4.

The mechanism for the ζ-circulation has not been identified. In Chapter 5 a possible mechanism for the ζ-circulation, involving the centrifugal force, is put forward. In a computer model it is possible to remove the centrifugal force term

from the dynamical equations whilst keeping all the other terms (including the Coriolis force term). Thus a comparison of computor simulations of the flow, with and without the centrifugal force term should provide a critical test of the role it plays in the ζ-circulation, assuming that the model is able to simulate the flow with sufficent accuracy.

The role of eddies in the advection of heat has not been effectively investigated so far. Sloping bases have previously proved effective in suppressing the formation of waves in unblocked annulus systems, see *Hide (1969), Mason (1972), (1975)* and *Hide and Mason (1975)*. If sloping bases suppress the eddies seen in the blocked system, then measurements of heat transport without eddies can be made over the complete range of Ω covered in the experiments. These heat transport measurements could then be compared with those recorded in *Figure 3.11* and *3.17* and *Table 3.2*, and calculated from the η and ζ-circulations. The investigations reported in Chapter 6 involve two types of sloping bases, and may allow the role of the eddies in the heat advection to be determined.

The heat advection of the eddies could also be calculated from the fluid temperature and velocity fields if simultaneous measurements of temperature and velocity could be made. These results could then be compared with the heat advection from the total heat transport measurements.